arXiv:astro-ph/0601548v1 24 Jan 2006

Version – 23/Jan/2006

Comparison of ^{13}CO Line and Far-Infrared Continuum Emission as a Diagnostic of Dust and Molecular Gas Physical Conditions: II. The Simulations: Testing the Method

W. F. Wall

Instituto Nacional de Astrofísica, Óptica, y Electrónica, Apdo. Postal 51 y 216, Puebla, Pue., México

wwall@inaoep.mx

ABSTRACT

The reliability of modeling the far-IR continuum to ^{13}CO J = 1 → 0 spectral line ratios applied to the Orion clouds (Wall 2006) is tested by applying the models to simulated data. The two-component models are found to give the dust-gas temperature difference, ΔT, to within 1 or 2 K. However, other parameters like the column density per velocity interval and the gas density can be wrong by an order of magnitude or more. In particular, the density can be systematically underestimated by an order of magnitude or more. The overall mass of the clouds is estimated correctly to within a few percent.

The one-component models estimate the column density per velocity interval and density within factors of 2 or 3, but their estimates of ΔT can be wrong by 20 K. They also underestimate the mass of the clouds by 40-50%.

These results may permit us to reliably constrain estimates of the Orion clouds' physical parameters, based on the real observations of the far-IR continuum and ^{13}CO J = 1 → 0 spectral line. Nevertheless, other systematics must be treated first. These include the effects of background/foreground subtraction, effects of the HI component of the ISM, and others. These will be discussed in a future paper (Wall 2006a).

Subject headings: ISM: molecules and dust — Orion

1. Introduction

Paper 1 (Wall 2006) examined the ability of the FIR-continuum to ^{13}CO J = 1 → 0 line intensity ratio to diagnose dust and molecular gas physical conditions. Specifically, the *COBE/DIRBE* 140 μm and 240 μm continuum data (see *COBE/DIRBE* Explanatory Supplement 1998) were compared with the Nagoya 4-m ^{13}CO J = 1 → 0 spectral line data for the Orion A (Nagahama et al. 1998) and B molecular clouds. The $I_\nu(240\,\mu\mathrm{m})/I(^{13}\mathrm{CO})$ ratio, or r_{240}, was plotted against the 140 μm/240 μm dust color temperature, or T_{dc}, for the high signal-to-noise positions ($\geq 5-\sigma$ for 140 μm, 240 μm, and ^{13}CO J = 1 → 0) in the Orion clouds. This plot was modeled with LTE and LVG, one-component models and LVG, two-component models; the two-component models fit the data better than the one-component models at the 99.9% confidence level. Tables 1, 2, and 3 of Paper I list the resultant parameter values of the two-component model fits. The most noteworthy result is that the two-component models demand the dust-gas temperature difference, ΔT, to be zero within $\pm$1 or 2 K. (Note that in the case of the two-component, two-subsample models, the $T_{dc} \geq 20$ K subsample still yields $\Delta T = 0 \pm 1$K *if* a two-component model is fitted to that subsample. The listed results in Table 2 of Paper I are those of the one-component model fitted to the $T_{dc} \geq 20$ K subsample.) This result has important consequences that were briefly mentioned in Paper I and will be discussed in detail in Paper III (Wall 2006a). Consequently, the reliability of the derived ΔT must be tested.

In all of the modeling mentioned in Paper I, the systematic uncertainties of the derived parameter values were evaluated by applying scale factors to the data. These systematic uncertainties are related to uncertainties in the calibration and in certain assumptions, such as the dust optical depth to gas column density ratio. The combined effect of these uncertainties was estimated to be $\pm$40%. Accordingly, scale factors that varied from 0.6 to 1.4 were applied to the data to see how strongly the resultant parameter values would change. Also, the starting search grid for the two-component models was slightly shifted and re-run. The magnitudes of the changes in the results provided another test of the systematic uncertainties in the parameter values. These two tests gave similar estimates of the systematic uncertainties. These systematic uncertainties are demonstrated in Figure 21 of Paper I, which shows that the column densities per velocity interval and densities of both components are uncertain by factors of a few or by more than an order of magnitude. (These uncertainties are orders of magnitude larger than the formal uncertainties obtained from the model fits. Accordingly, the latter uncertainties can be ignored.)

While the abovementioned tests provide rough estimates of the reliability of the results, they do *not* measure any biases inherent in the method. In other words, the range of possible parameter values that result from the modeling and from the tests *may not even include the*

"true" or correct value. And we cannot know that these ranges are indicative of the correct values, because we cannot know the correct values in the first place. This is in stark contrast to using simulated data. With simulated data, the true, or input, values can be compared with the resultant values from the model fits. The tests that were applied to modeling the actual observed data can be repeated on the modeling of the simulated data. Biases or shortcomings in the modeling technique are then clearly seen. In the following section and its subsections, the creation of the simulated data and the results of modeling these data is described.

Other systematics are not discussed in the current paper, but are left to Paper III. These are the systematic effects that result when the models do not properly characterize the contributions of other phases of the ISM, such as from HI and its dust or from some large-scale foreground/background emission, or when they adopt an improper value of some more basic physical parameter, such as the far-IR spectral emissivity index, β.

2. The Simulations

To better understand the strengths and weaknesses of determining gas and dust physical conditions using the ratio of the FIR continuum to the ^{13}CO J $= 1 \rightarrow 0$ line, simulated data were created. The simulations assumed that the real clouds are composed of two components: a component 0 and a component 1. The former has constant physical conditions; i.e., they do not vary from one line of sight to another. The latter also has constant physical conditions, except for the dust and gas temperatures (i.e. T_d and T_K). The component-1 temperatures vary from line of sight to line of sight, but maintain a constant dust/gas temperature difference, $\Delta T \equiv T_d - T_K$. The simulations started with a map of beam-averaged column densities (i.e., column densities that are averaged over $\sim 1^\circ$ scales) and component-1 dust temperatures. T_{d1}. Model parameters were specified for two subsamples and two components (see Table 1 for details). The two subsamples were the $T_{d1} < 20\,K$ points and the $T_{d1} \geq 20\,K$ points. This is not exactly the same as using $T_{dc} = 20\,K$ (where T_{dc} is the $140\,\mu m/240\,\mu m$ color temperature) as the boundary (as was done in Paper I), but, since $T_{d0} = 18\,K$ and since the column density of component 1 within each velocity interval, i.e. $\frac{N_{c1}}{\Delta v_c}$, is factors of 4 to 10 larger than the corresponding component-0 quantity, $\frac{N_{c0}}{\Delta v_c}$ (see Table 1), component 1 dominates the emission near the $T_{d1} = 20\,K$ boundary by roughly an order of magnitude. Consequently, $T_{dc} = 20\,K$ is equivalent to $T_{d1} = 20\,K$ for all practical purposes. The model intensity maps were then generated using the procedure below:

1. The map of T_{d1} values determined whether a given pixel belonged to subsample 1 or subsample 2.

2. The subsample to which a pixel belongs then dictated which model parameter values belonged to that pixel. Using these values in equation (28) of Paper I gave the area filling factor within a clump velocity width, or the c_1 value, for that pixel. The observed velocity width, Δv, adopted was $2\,\mathrm{km}\cdot\mathrm{s}^{-1}$, which is the the actual observed velocity width in the Orion clouds in the ^{13}CO J $= 1 \rightarrow 0$ line on the scale of 1°. Nevertheless, the expressions that give the observed intensities (i.e., 27 and 29 of Paper I) are actually independent of Δv. Δv only determines the filling factor, c_1.

3. Equations (20), (27), (31), (32), and (29) of Paper I then gave the $\mathrm{I}_\nu(140\,\mu\mathrm{m})$, $\mathrm{I}_\nu(240\,\mu\mathrm{m})$, and I(^{13}CO) intensities observable from that pixel. In addition, the color corrections for bands 9 and 10 of *COBE/DIRBE* converted the $\mathrm{I}_\nu(140\,\mu\mathrm{m})$ and $\mathrm{I}_\nu(240\,\mu\mathrm{m})$ values to those observable in the *DIRBE* bands.

4. The intensities, $\mathrm{I}_\nu(140\,\mu\mathrm{m})$, $\mathrm{I}_\nu(240\,\mu\mathrm{m})$, and I(^{13}CO), then specified the uncertainties in those intensities, $\sigma(140\,\mu\mathrm{m})$, $\sigma(240\,\mu\mathrm{m})$, and $\sigma(^{13}\mathrm{CO})$, based on the prescriptions described below and based on the observed data. These uncertainties for all the pixels represent the σ maps.

5. For the given pixel, a random number generator with a normally distributed probability of outputs with a mean of zero and an rms dispersion of unity generated noise values in the three wavelength bands. The noise value for each band was scaled by the σ for that pixel and for that band (i.e. $\sigma(140\,\mu\mathrm{m})$, $\sigma(240\,\mu\mathrm{m})$, or $\sigma(^{13}\mathrm{CO})$). These noise values for all the pixels represent the noise maps.

6. The noise maps were then added to the noise-free intensity maps to produce the final simulated maps.

The noise prescriptions mentioned above are based on the 3×3 smoothed maps of the real observations. The uncertainties in these maps had approximately the following behavior:

$$\sigma(140\,\mu\mathrm{m}) = \begin{cases} 2\,\mathrm{MJy}\cdot\mathrm{sr}^{-1}, & \text{for } \mathrm{I}_\nu(140\,\mu\mathrm{m}) \leq 60\,\mathrm{MJy}\cdot\mathrm{sr}^{-1} \\ 0.03\,\mathrm{I}_\nu(140\,\mu\mathrm{m}), & \text{for } \mathrm{I}_\nu(140\,\mu\mathrm{m}) > 60\,\mathrm{MJy}\cdot\mathrm{sr}^{-1} \end{cases} \tag{1}$$

$$\sigma(240\,\mu\mathrm{m}) = \begin{cases} 0.5\,\mathrm{MJy}\cdot\mathrm{sr}^{-1}, & \text{for } \mathrm{I}_\nu(240\,\mu\mathrm{m}) \leq 50\,\mathrm{MJy}\cdot\mathrm{sr}^{-1} \\ 0.01\,\mathrm{I}_\nu(140\,\mu\mathrm{m}), & \text{for } \mathrm{I}_\nu(240\,\mu\mathrm{m}) > 50\,\mathrm{MJy}\cdot\mathrm{sr}^{-1} \end{cases} \tag{2}$$

$$\sigma(^{13}\mathrm{CO}) = \begin{cases} 0.05\,\mathrm{K}\cdot\ \mathrm{km}\cdot\mathrm{s}^{-1}, & \text{outside Orion A Field} \\ 0.005\,\mathrm{K}\cdot\ \mathrm{km}\cdot\mathrm{s}^{-1}, & \text{inside Orion A Field} \end{cases} \tag{3}$$

It should be mentioned that the sigma levels for the simulated $240\,\mu$m and ^{13}CO maps are actually half of those of the actual observed maps. This reduction of the sigma levels in the simulated $240\,\mu$m and ^{13}CO maps was done to ensure a sufficient number of high-sigma

points. To generate the σ map for I(^{13}CO), a portion of the map area that would represent the lower-noise subfield within Orion A Field was chosen. The simulated maps were chosen to be 51 pixels $\times$ 51 pixels, a total of 2601 pixels and similar to that of the Orion fields: 2609. The area designated to have the lower noise of the Orion A Field consisted of two separate rectangular patches with a total of 156 pixels. One of the patches included a peak in the input column density map and the other patch included areas of low column density (see Figure 1). The patch with the column density peak also had a peak in the component-1 dust temperature. This was consistent with the actual observations.

Now the input column density and component-1 dust temperature maps must be specified. These maps are depicted in Figure 1. The maximum column density was chosen to be roughly the same as that of the observations (i.e., the two-component models): 5×10^{22} *H nuclei* $\cdot$ cm^{-2}. The column density map has two elliptical gaussians: one with a low peak that crudely represents the Orion Nebula Field and one with a high peak that crudely represents the main body of the Orion A molecular cloud. In the Orion Nebula field, the dust temperature rises with rising column density. Consequently, the component-1 dust temperature map has an elliptical gaussian peak corresponding to the low peak in the column density map. In the main body of the Orion A cloud, however, the dust temperature declines with increasing column density. Therefore, the temperature map has an elliptical gaussian *valley* corresponding to the high peak in the column density map. The component-1 temperatures range from 3 to 28 K. To ensure that a small minority of the pixels had sufficiently low temperature values, these values were placed in two patches on the left edge of the map (see lower panel of Figure 1). The procedure above was then implemented using the parameter values in the first two columns of Table 1 to yield the simulated maps.

Figures 2 to 5 show the results of the simulations along with some comparisons with the observations. Figure 2 shows the distribution of pixel intensities for the 140- and 240-μm continuum maps and for the ^{13}CO J $= 1 \rightarrow 0$ line map for both the simulations and observations. The pixels represented in the histograms are only those where $I_\nu(140\,\mu\mathrm{m})$, $I_\nu(240\,\mu\mathrm{m})$, and I(^{13}CO) are simultaneously greater than 5-σ. This corresponds to 1465 pixels for the simulations and 674 pixels for the observations. Even after normalizing for the factor of $\sim$2 greater number of high signal-to-noise pixels in the simulations, the number of medium- and high-intensity pixels (i.e. $\gtrsim 200\,\mathrm{MJy \cdot sr^{-1}}$ for $I_\nu(140\,\mu\mathrm{m})$ and $\gtrsim 100\,\mathrm{MJy \cdot sr^{-1}}$ for $I_\nu(240\,\mu\mathrm{m})$) in the 140- and 240-$\mu m$ simulated maps is about 2 to 3 times higher than for the maps of the real observations. For the I(^{13}CO) map, the simulations have about a factor of 5 higher number of pixels of medium- and high-intensity (i.e. I(^{13}CO)$\gtrsim 2\,\mathrm{K \cdot km \cdot s^{-1}}$) than in the observations. All the simulated maps have a higher ratio of medium- and high-intensity pixels to low-intensity pixels than the observations. This is especially true for the ^{13}CO J $= 1 \rightarrow 0$ maps. This is partly because the simulations have roughly twice the fraction

of low r_{240} values than do the observations (i.e. for $r_{240} \lesssim 20\,\mathrm{MJy \cdot sr^{-1} \cdot (K \cdot km \cdot s^{-1})^{-1}}$). Nevertheless, the normalized pixel distributions of the simulations agree with those of the observations to within factors of a few. Exact agreement is not necessary in any case, because the purpose of the simulations is to check how well the original input parameters are recovered, whether those parameters adequately mimic the real observations or not.

Another check of this mimicry is given in Figure 3. These are the plots of r_{240} versus T_{dc} upon which all of the modeling in the current work is based. The simulations adequately reproduce the main features of the observations: the triangular cluster of points for $T_{dc} \lesssim 21\,\mathrm{K}$ and the monotonic rise for $T_{dc} \gtrsim 20\,\mathrm{K}$. However, the simulations do *not* account for the observed points that fill in the center of the triangular cluster and also do *not* account for the points of $r_{240} \gtrsim 80\,\mathrm{MJy \cdot sr^{-1} \cdot (K \cdot km \cdot s^{-1})^{-1}}$. This comparison between simulations and observations suggests that the basic assumption (see Paper I) is not correct and that we need appropriately chosen subsamples, each with its own set of physical conditions, to account for the shortcomings in the simulations (see the end of Section 3.4 of Paper I). Nevertheless, the simulated r_{240} versus T_{dc} plot is an adequate representation of the observations. In fact, the noise in the simulations seems to account for the low-r_{240} points (i.e. the points with $T_{dc} = 18$ to $22\,\mathrm{K}$ and $r_{240} \lesssim 15\,\mathrm{MJy \cdot sr^{-1} \cdot (K \cdot km \cdot s^{-1})^{-1}}$) mentioned in Section 3.1 of Paper I.

Figure 4 further compares the simulations with the observations, and has plots of the one-component, continuum-derived gas column densities, $N_d(H)$, versus the dust temperature, T_d, in the one-component case. Since these are continuum-derived quantities, they are independent of the particular parameter values of the one-component model (e.g., gas density, gas column density per velocity interval, etc.). Again, the simulations adequately imitate the observations. There are only slight differences. For example, the simulations show a hook-like feature centered at $T_d \simeq 17.5$, $N_d(H) \simeq 100$, which is nearly, but not completely, absent from the observations. Another example is a spur that extends from $T_d \simeq 14.3$ to 18 for $N_d(H) \simeq 15$ in the simulations that is only hinted at in the observations. Notice also that the simulations have a smaller vertical spread in the $T_d > 20\,\mathrm{K}$ points than do the observations. Still, these are just minor discrepancies.

Like Figure 4, Figure 5 plots the continuum-derived gas column densities against the dust temperature (the component-1 temperature for this figure), but this time for the two-component, two-subsample models. For the two-component cases, the specific parameter values *do* indeed matter. Specifically, the resultant parameter values from the model fits to the actual observations are those given in Table 2 of Paper I. The resultant parameter values from model fits to the simulations are given in Table 1 (the model results from the data with noise). Again, the simulations satisfactorily represent the observations and have only minor discrepancies. The most noticeable of these is the group of points with large error bars at

$T_{d1} = 3$ to 8 for $N_d(H) \simeq 150$ to 500 that occur for the real observations and are not in the simulations.

Given that the simulations are reasonable, we now examine how well the models recover the inputs. We start with the most realistic models — the two-component, two-subsample, LVG models — and move towards the simplistic models — the one-component models — to see what information they can realistically recover.

2.1. Two-Component, Two-Subsample Models of the Simulations

The best fitting model curves to the simulations for the two-component, two-subsample models are shown in Figure 6 and the corresponding parameter values are given in the last four columns of Table 1. Columns 4 and 5 of Table 1 list the model results from fitting the models to the data before the noise was added — i.e., the noise-free data. Columns 6 and 7 list those results for the fits to the data that have noise added. The results in these columns can be compared with the simulation inputs in columns 2 and 3. (Column 1 gives the parameter names.) The two subsamples were chosen from those pixels for which the signal-to-noise ratio was ≥ 5 in $I_\nu(140\,\mu m)$, $I_\nu(240\,\mu m)$, $I(^{13}CO)$ simultaneously. Of course, the signal-to-noise ratio is not defined for the noise-free maps; so the pixels that matched the signal-to-noise criteria in the maps with the added noise were also the pixels chosen in the corresponding noise-free maps. Also, fitting the model required specifying the error bars, even for the noise-free maps. The error bars were specified to be the same as those in the corresponding maps with added noise, even though the noise-free maps had no noise and, therefore, no errors.

A number of important conclusions result from comparing the results with the inputs. The most important is that **completely** *recovering the inputs* **even** *in the noise-free case is* **not** *possible.* This despite the model curves fitting the data extremely well (see Figure 6). Accordingly, problems like not recovering the correct values of c_0, n_{c0}, or n_{c1} within an order of magnitude or more are *intrinsic shortcomings* of the method itself and are *not* entirely due to the uncertainties caused by noise in the data. Also note that some results are *more* accurate in the noise-*added* data than in the noise-free data. For example, c_0 for both the $T_{dc} < 20\,K$ and $T_{dc} \geq 20\,K$ subsamples was more accurately recovered in the model fits to the data with noise than in fits to the noise-free data. This is also the case for $\frac{N_{c0}}{\Delta v_c}$ for the $T_{dc} < 20\,K$ subsample. Better recovery from fits to the data with noise is probably just random luck. As discussed in Section 3.3 of Paper I, the fitting process itself has random elements, such as the choice of starting grid. This choice affects the final results of some parameters. Consequently, a different choice of starting grid could easily result in worse

recovery than better.

Comparing the particular model results found here with the inputs gives a crude measure of the accuracy of the modeling. The results of this comparison are summarized below:

- ΔT is within 1 K for the $T_{dc} < 20$ K subsample and within 2 K for the $T_{dc} \geq 20$ K subsample (within 1 K in the noise-free case).
- T_{d0} for the $T_{dc} < 20$ K subsample is known within the formal uncertainty of $\leq 1 \times 10^{-5}$ K. (For the actual observations this would be an order of magnitude larger.) For the $T_{dc} \geq 20$ K subsample, the value for T_{d0} is adopted.
- c_0 is known within a factor of 2 for the $T_{dc} < 20$ K subsample (within a factor of 16 for the noise-free case). It is known within a factor of 3 for the $T_{dc} \geq 20$ K subsample (within a factor of 2 for the noise-free case).
- $\frac{N_{c0}}{\Delta v_c}$ is known within a factor of 3 for both subsamples (within a factor of 10 for the noise-free case for the $T_{dc} < 20$ K subsample and within a factor of 2 for the noise-free case for the $T_{dc} \geq 20$ K subsample).
- Again, the product $c_0 \frac{N_{c0}}{\Delta v_c}$ is more accurately recovered than either of its factors. This is known to within a factor of 2 for both subsamples (also within a factor of 2 or exactly correct in the noise-free case depending on the subsample).
- n_{c0} is out by 3 orders of magnitude or exactly correct depending on the subsample (with the same behavior in the noise-free case).
- $\frac{N_{c1}}{\Delta v_c}$ is within a factor of 2 for both subsamples (within a factor of 2 or exactly correct in the noise-free case depending on the subsample).
- n_{c1} is within a factor of 6 for the $T_{dc} < 20$ K subsample and within a factor of 2 for the $T_{dc} \geq 20$ K subsample (within a factor of 6 or exactly correct in the noise-free case depending on the subsample).

We discuss these accuracies in more detail after examining the results of simple two-component models applied to the simulated data in the next subsection.

One important point is the reliability of the ΔT result. Given that the two-component model results *always* yield a ΔT value that is within 1 K, or sometimes 2 K, of zero, is it *possible* that the two-component models *always* yield this result, *regardless of the true value of* ΔT*?* This was tested by modeling simulated maps with inputs $\Delta T = 8$ K for the $T_{dc} < 20$ K subsample and $\Delta T = 10$ K for the $T_{dc} \geq 20$ K subsample. *The two-component,*

two-subsample model results were again within 1 K of the input ΔT *values.* Therefore, ΔT is very likely zero for the observations as well.

The best fitting model curves can find the component-1 dust temperatures and the column densities as a function of position. These are compared with the original input values. Figure 7 shows the recovered T_{d1} values plotted against the input T_{d1} values. Despite the noise in the simulated maps, the recovered T_{d1} values match the input values to within a few percent for the majority of (high signal-to-noise) points. The most noticeable exceptions occur in two spurs that extend above and below the solid line plotted in the lower panel of that figure. The upper spur represents those positions where T_{d1} is between about 3 and 8 K, but has been misidentified as being between 16 and 9 K. The lower spur represents another misidentification of T_{d1}, but in the opposite sense: T_{d1} is really between 17 and 20 K, but has been assigned to be between 4 and 3 K. This mistake in assigning the correct T_{d1} value for some positions is easy to understand. In Figure 6, the model curve for the $T_{dc} < 20$ K sample crosses itself; there is a vertical segment that crosses an inclined segment. At the intersection point, the vertical segment has $T_{d1} \simeq$ 3-4 K and the inclined segment has $T_{d1} \simeq 18$ K. Therefore, any points in the r_{240} versus T_{dc} plot near this intersection point are easily misassigned to the vertical segment, when it really belongs to the inclined segment, and vice versa. As the noise in the data grows larger, more points will be assigned to the wrong segment. In this case, the number of misassigned points is only 8% of the total number of high signal-to-noise points.

The misassignment of T_{d1} values changes the determination of column densities. This is illustrated in the panels of Figure 8, which are plots of the model-derived column densities (i.e., continuum-derived gas column densities and ^{13}CO line-derived gas column densities) versus the input column densities. As in the previous figure, the majority of positions show nearly perfect agreement (within a few percent) between the model-derived column densities and the input column densities. However, again as in the previous figure, there are two spurs representing strong disagreements. In this figure the disagreements are factors of $\sim$4-6 in either direction. Obviously, the spurs in the column density plots of Figure 8 correspond to the spurs in the dust temperature plots of Figure 7, although in the opposite sense: the upper spur in the dust temperature plots corresponds to the lower spur in the column density plots and vice versa. The question is why the disagreements are around a factor of 5. Starting with equation (40) of Paper I, we first consider the case where the T_{d1} of a position is 18 K, which is numerically equal to T_{d0}, and has been misassigned to 4 K. If the T_{d1} value had been correct, then the correct column density *would* have been given by

$$N_d(H)(\text{correct}) = \frac{f_{\nu_{10}}(T_{dc})}{f_{\nu_{10}}(T_{d0})}\, N_{d1}(H) \qquad , \tag{4}$$

which was obtained by setting $T_{d1} = T_{d0}$. This in turn implies $T_{dc} = T_{d0}$ and (4) simplifies

to

$$\mathrm{N_d(H)(correct) = N_{d1}(H)} \qquad . \tag{5}$$

But, because this data point has $\mathrm{T_{d1}}$ misassigned to some low value, we have

$$\mathrm{N_d(H)(incorrect)} \simeq \frac{\left[\frac{\mathrm{N_{c1}(^{13}CO)}}{\Delta \mathrm{v_c}}\right]_{mod} + \mathrm{c_0}\left[\frac{\mathrm{N_{c0}(^{13}CO)}}{\Delta \mathrm{v_c}}\right]_{mod}}{\mathrm{c_0}\left[\frac{\mathrm{N_{c0}(^{13}CO)}}{\Delta \mathrm{v_c}}\right]_{mod}} \; \frac{\mathrm{f}_{\nu_{10}}(\mathrm{T_{dc}})}{\mathrm{f}_{\nu_{10}}(\mathrm{T_{d0}})} \; \mathrm{N_{d1}(H)} \qquad , \tag{6}$$

where $f_{\nu_{10}}(\mathrm{T_{d1}}) << \mathrm{f}_{\nu_{10}}(\mathrm{T_{d0}})$ was assumed. This assumption is especially valid in the Wien limit, which applies to the 240 μm continuum for these temperatures. Because the Wien limit applies, we can also state that $\mathrm{T_{dc}} \simeq \mathrm{T_{d0}}$, so that $f_{\nu_{10}}(\mathrm{T_{dc}}) \simeq \mathrm{f}_{\nu_{10}}(\mathrm{T_{d0}})$. Using this and dividing (6) by (5) yields

$$\frac{\mathrm{N_d(H)(incorrect)}}{\mathrm{N_d(H)(correct)}} \simeq \frac{\left[\frac{\mathrm{N_{c1}(^{13}CO)}}{\Delta \mathrm{v_c}}\right]_{mod} + c_0\left[\frac{\mathrm{N_{c0}(^{13}CO)}}{\Delta \mathrm{v_c}}\right]_{mod}}{c_0\left[\frac{\mathrm{N_{c0}(^{13}CO)}}{\Delta \mathrm{v_c}}\right]_{mod}} \qquad . \tag{7}$$

Using the parameter values in Table 1 for the $\mathrm{T_{dc}} < 20\,\mathrm{K}$ subsample for the data with noise gives $\mathrm{N_d(H)(incorrect)/N_d(H)(correct)} \simeq 5$ as desired. For the real observed data, the model parameter values in Table 2 again give $\mathrm{N_d(H)(incorrect)/N_d(H)(correct)} \simeq 5$. Note that in the opposite case where the $\mathrm{T_{d1}} = 4\,\mathrm{K}$ data point is misassigned to $\mathrm{T_{d1}} = 18\,\mathrm{K}$, the right side of expression (7) is changed to its reciprocal or, numerically, 0.2. Even though there are two spurs, there are many more points in the upper spur than in the lower spur; this results in overestimate of the total mass of about 7%.

The above only explains the spur locations in the continuum-derived column density plots of Figure 8 (i.e., the upper panels). The explanation for the ^{13}CO-derived column densities is similar. Instead of starting with expression (40) of Paper I as was done for the continuum-derived column densities, we would start with (34) of Paper I. Since $\mathrm{T_R} \propto \mathrm{N(^{13}CO)}/\Delta\mathrm{v}$ for a large area of parameter space (see Section 3.3 of Paper I), the arguments used above apply to the ^{13}CO-derived column densities as well. The only difference is that, now, the Wien limit does not apply and we may not be able to approximate the $(\mathrm{T_{R1}}+c_0\mathrm{T_{R0}})$ in the denominator with $c_0\mathrm{T_{R0}}$. Nevertheless, such an approximation is *still* valid, because these radiation temperatures are with respect to the cosmic background temperature of roughly 3 K. So, for the example discussed here, where $\mathrm{T_{d1}} = 18\,\mathrm{K}$ is mistaken for $\mathrm{T_{d1}} = 4\,\mathrm{K}$, $\mathrm{T_{R1}/T_{R0}}$ is not $\frac{4}{18}$, but closer to $\frac{1}{15}$, more than 3 times smaller. Consequently, equation (7) and its reciprocal are still valid for the ^{13}CO-derived column densities. The overestimate of the total mass from using the ^{13}CO data is similar to that for the continuum-derived total mass: 6%.

Figure 9 shows that the two types of model-derived column densities agree with each other extremely well, *despite* having 7% of these wrong by factors of 5. The total masses also agree well because the erroneous column densities are wrong by the same factors for both the continuum-derived and ^{13}CO-derived column densities.

In summary, the simulations show that even modeling the noise-free data will not allow perfect recovery of the parameters. Nevertheless, the simulations show that we obtain ΔT to within 1 or 2 K (even when that ΔT is different from zero), T_{d0} to better than a millikelvin for the $T_{dc} < 20$ K subsample, the component-0 density can be off by 3 orders of magnitude, and the other parameters might be known to within about an order of magnitude. Recovery of other quantities like the component-1 dust temperatures and the gas column densities is apparently accurate to within a few percent for 93% of the points. The other 7% of the points have column densities too high or too low by a factor of about 5. This results in overestimate of 6-7% in the total mass.

2.2. Simple Two-Component Models of the Simulations

The best fitting model curve for the two-component models applied to the whole sample of high signal-to-noise points in the simulations is shown in Figure 10. Again, these points corresponded to those pixels for which the signal-to-noise ratio was $\geq$ 5 in $I_\nu(140\,\mu\mathrm{m})$, $I_\nu(240\,\mu\mathrm{m})$, I(^{13}CO) simultaneously. As done in Section 3.3 and Figure 21 of Paper I, Figure 11 shows the systematic effects on the resultant parameters when a scale factor applied to the data is changed. Comparing the various panels of Figure 11 with the corresponding panels of Figure 21 of Paper I reveals strong similarities between the models applied to the simulations and those applied to the observed data. The range of parameter variations is nearly identical in the two cases. However, there is one important difference between the systematic effects on the simulated data model results and those of the observed: with the simulated data we can specify the accuracy of the recovered results by comparing the "true" values (i.e., the inputs) with the model results; with the actual observed data we can only estimate such accuracy by comparing the results in different cases (i.e., with different scale factors applied to the data or with different starting grids) with each other. The accuracy of the recovered results for the simulations can also be tested by comparing the results in different cases — as was done in Figure 11. By comparing this accuracy with the accuracy obtained from comparisons with the input values, we now have insights into the estimated accuracies of the actual observations.

An example of such comparisons is inspecting how ΔT varies in Figure 11 about the ΔT value for a scale factor of unity (i.e. SF=1.0) and then comparing this with how those

ΔT values vary about the original input value. This then tells us whether the variation of ΔT with the scale factor for the real observations (see Figure 21 of Paper I) is a realistic measure of the uncertainty in ΔT. In Figure 11, ΔT varies within 2 K of the value, i.e. $\Delta T = 0$ K, for SF=1.0. The input value was $\Delta T = 0$ K. Therefore, the variation of ΔT with the scale factor provides a reasonable estimate of the actual uncertainty in ΔT. For the models applied to the observations, Figure 21 of Paper I shows us that ΔT varies within 1 K of the value corresponding to SF=1.0, i.e. $\Delta T = 0$ K. So we can say that the model ΔT value is within 1 or 2 K of the true ΔT value. Using the same arguments applied to T_{d0} suggests that this is known to within a 1 mK or less; this is undoubtedly optimistic and is dependent on the basic assumption. (It is also dependent on other assumptions, such as whether the spectral emissivity index, β, really is 2.0 or something nearby. Paper III suggests that T_{d0} can be anywhere from $\sim$16 to $\sim$19 K.) For the other parameters, which had different input values for the two subsamples, we will compare the model results with the geometric mean of the two inputs:

- The parameter c_0 can be off by a factor of 10 from the value corresponding to SF=1.0 (for both the simulations and the observations), but is off by a factor of 40 from the input. In addition, the model-derived c_0 values for all the scale factors are systematically lower than the input. In other words, we cannot rely on varying the scale factor to give us parameter values that will surround the true value. Again, c_0 is much more reliable when combined with $\frac{N_{c0}}{\Delta v_c}$.

- $\frac{N_{c0}}{\Delta v_c}$ itself can be out by a factor of 100 from the value corresponding to SF=1.0 (for both simulations and observations), *and* is *also* wrong by this factor compared to the input.

- The product $c_0 \frac{N_{c0}}{\Delta v_c}$ is off by at most only a factor of 10 compared to the value corresponding to SF=1.0, *and* is *also* wrong by this factor compared to the input. Also, unlike c_0 alone, the range of different values of $c_0 \frac{N_{c0}}{\Delta v_c}$ corresponding to different scale factors does indeed include the input value.

- n_{c0} is as much as a factor of 100 away from the value for SF=1.0 for the simulations, and as much as factor 1000 away for the observations. The different n_{c0} values for the simulations can be wrong by as much as a factor of 200 from the input, and the range of these values includes the input value. It would seem, then, that the observations would suggest a greater uncertainty in n_{c0} than would the simulations.

- $\frac{N_{c1}}{\Delta v_c}$ is as much as a factor of 10 from the value at SF=1.0 for both the simulations and observations. $\frac{N_{c1}}{\Delta v_c}$ can be as far as a factor of 30 from the input, which is worse than

the comparison with the $\frac{\mathrm{N_{c1}}}{\Delta \mathrm{v_c}}$ value at SF=1.0 would suggest. The range of possible $\frac{\mathrm{N_{c1}}}{\Delta \mathrm{v_c}}$ values for the different scale factors (see Figure 11) includes the input value.

- n_{c1} can be as far as a factors of 2 or 3 from the value at SF=1.0 for both the simulations and observations. However, n_{c1} can be out by a factor of 20 from the input value, much worse than comparison with the value at SF=1.0 implies. Also, another problem is that the range of possible n_{c1} values (see Figure 11) does *not* include the input: the model-derived densities are all systematically too low by more than an order of magnitude.

The most interesting conclusion is that some parameters like c_0 and n_{c1} have a range of values that does *not* include the true input value. As mentioned previously, c_0 is assessed more reliably as part of the $c_0 \frac{\mathrm{N_{c0}}}{\Delta \mathrm{v_c}}$ product, whose range of values does indeed include the input value. n_{c1} still has this disadvantage, which cannot be "fixed" as easily as for c_0.

Based on the comparisons of the different results, the ranges of likely values of the different parameters have been listed in Table 2. The range of values for each parameter assumes the minimum and maximum values as in the case of the simple, and the two-subsample, two-component models — with some important exceptions. In the case of ΔT, the maximum value found was +1 K, but the simulations suggest that +2 K is also possible. Therefore, +2 K is listed. Note also that even though, for simplicity, a one-component model was applied to the $\mathrm{T_{dc}} \geq 20\,\mathrm{K}$ subsample, the two-component model results for that subsample represent the likely ranges listed in Table 2. For c_0 and $\frac{\mathrm{N_{c0}}}{\Delta \mathrm{v_c}}$, only the range of their product was listed, in order to provide more realistic constraints on these parameters. For the column density per velocity interval in general, it was stated in Section 3.2 of Paper I that the lower limit had to be about $3 \times 10^{15}\ {}^{13}CO\ molecules\ \mathrm{cm}^{-2} \cdot (\mathrm{km} \cdot \mathrm{s}^{-1})^{-1}$ as roughly constrained by the large-scale properties of the cloud. For the two-component models, this lower limit would apply to $\frac{\mathrm{N_{c1}(^{13}CO)}}{\Delta \mathrm{v_c}} + c_0 \frac{\mathrm{N_{c0}(^{13}CO)}}{\Delta \mathrm{v_c}}$. However, $\frac{\mathrm{N_{c1}(^{13}CO)}}{\Delta \mathrm{v_c}}$ is larger than $c_0 \frac{\mathrm{N_{c0}(^{13}CO)}}{\Delta \mathrm{v_c}}$ by factors of 3 to 4. Therefore, the first term in that expression dominates and it is sufficient to apply that lower limit to $\frac{\mathrm{N_{c1}(^{13}CO)}}{\Delta \mathrm{v_c}}$ only, as was done in Table 2. As for the densities, n_{c0} and n_{c1}, putting upper limits on those is not possible, because the results are not distinguishable from those of LTE. Consequently, only lower limits are used. Also the lower limit of n_{c1} has been increased by an order of magnitude, because, as stated in the previous paragraph, all the values of n_{c1} found by the simple two-component models are too low by at least an order of magnitude.

The best fitting model curves shown in Figure 10 were used to find the component-1 dust temperatures and the column densities as a function of position. These are compared with the original input values. Figure 12 shows the recovered $\mathrm{T_{d1}}$ values plotted against the input $\mathrm{T_{d1}}$ values. Again, as in Figure 7, the majority of recover $\mathrm{T_{d1}}$ values match the input values reasonably well, except for the two spurs. The noticeable difference, however, is the

systematic overestimate of T_{d1} for input T_{d1} values $\lesssim 20\,K$ and a systematic underestimate of most of the T_{d1} values above this limit. These systematic effects are obviously the result of forcing a single curve to fit the two different subsamples: the curve systematically underestimates a large fraction of the $T_{dc} < 20\,K$ subsample and overestimates most of the $T_{dc} \geq 20\,K$ subsample. This results in systematically underestimating (overestimating) the T_{d1} values for the simulated data points in the $T_{d1} < 20\,K$ ($T_{dc} \geq 20\,K$) subsample.

The incorrect estimates of the T_{d1} values change the determination of the column densities. This is obvious in the panels of Figure 13, which are plots of the model-derived column densities versus the input column densities, analogous to those in Figure 8 for the two-component, two-subsample models. As in Figure 8, there are two spurs of very large disagreements (i.e., factors of ~ 5 in both directions). But, unlike that figure, Figure 13 shows systematic disagreements of about 10% and 20% on either side of the solid line — the line that represents perfect agreement. Again those disagreements follow naturally from the disagreements seen in the plot of T_{d1} values in Figure 12: the points that have overestimated T_{d1} values in the $T_{dc} < 20\,K$ subsample will have underestimated column densities and vice versa for many of the points in the $T_{dc} \geq 20\,K$. Despite these noticeable disagreements, the continuum-derived and ^{13}CO-derived column densities in Figure 14 agree well, although with noticeably larger scatter than in Figure 9 for the two-component, two-subsample models. Also, the total mass estimated from the model results is only overestimated by about 3 to 6%.

In summary, the results of the simple two-component models applied to the simulations for different scale factors has allowed reasonable estimates of the ranges of parameter values for all the two-component models. These ranges allow for systematic uncertainties in the real observations and are listed in Table 2. There are noticeable systematic errors in the derived component-1 dust temperatures and in the derived column densities. Despite these systematic errors, the simple two-component models still give reasonable estimates of the total mass of the Orion clouds.

2.3. One-Component, Non-LTE Models of the Simulations

The best fitting model curve for the one-component models applied to the high signal-to-noise points in the simulations is depicted in Figure 15. As discussed in Section 3.2 of Paper I and illustrated in Figure 16 of Paper I, Figure 16 of the current paper shows the systematic effects on the resultant parameters when a scale factor applied to the data is changed. Comparing the three panels of Figure 16 with the corresponding panels of Figure 16 of Paper I reveals that the models of the simulations and those of the observed

data are similar. The range of variation of the parameters is nearly identical in the two cases, except in the panels of the ΔT values: in that panel the model results of the simulations have systematically lower ΔT values than those of the observations by 1 to 5 K, the larger difference applying to the $T_d \geq 20$ K subsample. For this subsample, the observed data points have lower r_{240} values on average than do the simulated data points.

Also, the one-component modeling of the observed data was done a little differently from that of the simulated data. The observed data were modeled with the one-component models applied to the whole sample of points and then again for just the $T_d \geq 20$ K points. In contrast, the simulated data were modeled with the one-component models applied to *just* the $T_d < 20$ K points and then *just* the $T_d \geq 20$ K points. In short, the $T_d < 20$ K subsample was *not* treated separately for the observed data points, but was indeed treated separately for the simulated data points. This different treatment is because the $T_d \geq 20$ K subsample only represents 12% of the high signal-to-noise points in the observed data, but represents 28% of those points in the simulated data. Therefore, modeling the entire sample of observed data points yields results that are nearly identical to modeling only the $T_d < 20$ K subsample, because these points are the majority of data points. For the simulated data, this is not entirely the case, because the $T_d \geq 20$ K subsample is not such a negligible fraction of the complete sample; therefore completely separating the two subsamples was more important for the simulated data than for the observed data.

Now the model results are compared with the inputs. The model-derived ΔT values are all systematically lower than the input ΔT values. For the $N(^{13}CO)/\Delta v$ and $n(H_2)$ parameters, we must find the corresponding parameters in the two-component, two-subsample models (because these were the models used to generate the simulated maps). The continuum emission of the majority of points in the $T_d < 20$ K subsample are dominated by the emission of component 0 and the continuum emission of all of the points in the $T_d \geq 20$ K subsample are dominated by the emission of component 1. *However,* since the parameters we are discussing are largely physical parameters of the molecular gas, the ^{13}CO $J = 1 \rightarrow 0$ line emission is a better guide in determining which component is the more relevant. The ^{13}CO $J = 1 \rightarrow 0$ line emission of component 1 dominates that of component 0 for *all* the points, except for the small minority of points where the component 1 temperature is less than about 4 K. Therefore, the $N(^{13}CO)/\Delta v$ and $n(H_2)$ values of the one-component models are identified with the $\frac{N_{c1}}{\Delta v_c}$ and n_{c1} values of the two-component models for both subsamples. The resultant $N(^{13}CO)/\Delta v$ values compare very favorably with the known input values: the range of $N(^{13}CO)/\Delta v$ values includes the input values of $\frac{N_{c1}}{\Delta v_c}$ for the $T_d < 20$ K and the $T_d \geq 20$ K subsamples. Also four of the five $N(^{13}CO)/\Delta v$ values for the different SF values are within a factor of 2 of the input value for the $T_d \geq 20$ K subsample. The densities determined from the one-component models cover ranges that include the input values. At

SF=1.0, the model density is within a factor of 2 of the input n_{c1} value of the $T_d \geq 20\,K$ subsample. Even though the one-component model curves do not characterize the data well, it is ironic that some parameter values, like the column density per velocity interval and the volume density, are obtained more accurately with the one-component, two-subsample models than with the simple two-component models. It is clear then that, for some parameters, there is a greater advantage in having two subsamples than there is in having two components. This may be an effect of using the continuum emission, because the two subsamples *almost* correspond to the two separate components when we consider just the continuum emission.

The best fitting model curves in Figure 15 were used to find the dust temperatures and the column densities as a function of position. Figure 17 shows the recovered T_d values plotted against the input T_{d1} values. As expected, the model T_d values do not reproduce all the input T_{d1} values, except for high T_{d1}. Above $T_{d1} \simeq 16\,K$, the model T_d values are within about 1 K of the input T_{d1} values. Below this temperature, the one-component T_d values increase with *de*creasing T_{d1}. This is because, as T_{d1} decreases, component 0 and its temperature increasingly dominate the emission. Also visible are two areas of larger error bars and, consequently, of heightened noise (i.e. more scatter), located at $T_{d1} \lesssim 7\,K$ and at $T_{d1} \simeq$ 19-21 K. This is due to the relatively larger noise at these temperatures in all three simulated maps (i.e., the maps of $I_\nu(140\,\mu m)$, $I_\nu(240\,\mu m)$, and $I(^{13}CO)$).

The incorrectly determined T_{d1} values adversely affect the determination of the column densities. This is obvious in the panels of Figure 18, analogous to the plots in the previous subsections. To explain these plots we consider three groups of points defined in terms of the plots that appear in Figure 5. The separate group of points that occur between $T_{d1} = 3$ and 7 K for all values of $N_d(H)$ and for T_{d1} between about 7 and 17 K for $N_d(H) \lesssim 50$ will be called "Group 1". The long descending (as one moves left to right) curve of points that starts at $T_{d1} \simeq 7$ or 9 K (for the simulations and observations, respectively) with $N_d(H) = 550$ and runs down to $T_{d1} \simeq 20\,K$ with $N_d(H) \simeq 10$ will be called "Group 2". The final ascending curve of points beyond $T_{d1} \simeq 20\,K$ is "Group 3". In the panels of Figure 18, Group 1 is the lower spur of points that runs from about (0,0) to about (100,20). This spur corresponds to the lower spur in the column density plots of Figures 8 and 13; as explained previously, the strong underestimates of the column densities represented by this spur is due to the strong overestimates of the dust temperatures: component-0 emission overwhelmingly dominates over component-1 emission when this latter component is so cold. Assuming a single component in the modeling will then result in a dust temperature that is the component-0 dust temperature. For the ^{13}CO-derived column densities, Group 3 is the group of points that runs along the slope=1 line. The nearly perfect agreement here is because the dust temperatures for this group are correct to within a fraction of a Kelvin.

Group 2 is the long curve that runs from the origin to the upper right of the plot in the panels for the ^{13}CO-derived column densities. As one ascends this curve (moving from left to right), the column density estimates move increasingly further from the correct (i.e., input) column densities. In Figure 17, Group 2 is the flattened V-shaped curve of points that extends from $T_{d1} \simeq 7\,K$ to $20\,K$. As one moves to lower T_{d1}, the model T_d moves further from the input T_{d1}. And, as one moves to lower T_{d1} in Figure 17, one is moving to higher $N_{13}(H)$ in Figure 18. Consequently, the model T_d moving further from the input T_{d1} is the reason that the model $N_{13}(H)$ moves further from the input N(H). Another noticeable characteristic of the curve (of the points in Group 2) in the lower panels of Figure 18 is that its slope increasingly deviates from unity when moving left to right and then, for input $N(H) \gtrsim 360$, the slope curves back in the direction of slope=1. This is simply a reflection of the flattened V-shaped curve in Figure 17 when moving right to left. The upper panels of Figure 18, which have the continuum-derived column densities, show more extreme deviations of the one-component-model column densities from the input column densities. These panels also show qualitatively similar, but more extreme, slope variations in the Group 2 points than in the lower panels. This is because these continuum observations, at wavelengths close to the Wien limit, are much more sensitive to errors in the temperature estimates. Note also that the Group 2 and Group 3 points are blended in the upper panels for $N_d(H) \lesssim 100$ because of the higher uncertainties of some of the $140\,\mu$m observations compared with some of the ^{13}CO observations. Because of the greater sensitivity of the continuum observations to errors in temperature, the error in the estimated total gas mass is further from the correct value than that estimated from the ^{13}CO observations: the simulated continuum observations underestimate the total mass by 48% and the simulated ^{13}CO observations underestimate this mass by 40%.

Figure 19 has the plots of the ^{13}CO-derived column densities versus the continuum-derived column densities. In these plots, the disagreement is no worse than a factor of 2 to within about 5% for the majority of points with $N_d(H) \gtrsim 10$. The overall shape of the points, roughly reminiscent of the Loch-Ness monster, roughly reflects the points in the upper panels of Figure 18 about a solid line with slope=1 and intercept=0. A better description is that the points in Figure 19 represent a reflection of the points in the upper panels of Figure 18 about the corresponding groups of points in the lower panels of that figure. The slopes represented in Figure 19, again for the points with $N_d(H) \gtrsim 10$, range between about 0.8 and about 2. For the one-component models applied to the real data, the slopes range from about 0.6 and 1.7 (see Figure 10 of Paper I).

In summary, the one-component models can provide reasonable estimates of the column density per velocity interval and volume density (i.e., within factors of 2 or 3) provided that these models are applied to the two different subsamples (i.e. with T_d below and above

20 K); these reasonable numerical estimates are possible despite the poor characterization of the r_{240} versus T_d data points by the one-component models. The estimates of ΔT, however, can be wrong by about 20 K. The one-component models result in mass estimates that are too low by about 40-50%; the continuum-derived mass estimates being worse on average than the ^{13}CO-derived mass estimates due to the higher temperature sensitivity of the continuum observations.

3. Summary and Discussion

The reliability of recovering physical conditions in the dust and gas of molecular clouds using the far-IR continuum and the ^{13}CO $J = 1 \rightarrow 0$ line was tested by using simulated data. These data were created using input beam-average column density and dust temperature maps that crudely represented the inferred physical conditions in the Orion A and B giant molecular clouds (see Paper I Wall 2006). Input physical parameters, with values similar to those recovered from modeling the actual observed data (see Paper I), in combination with the column density and dust temperature maps gave us the simulated intensity maps in the 140 μm continuum, 240 μm continuum and ^{13}CO $J = 1 \rightarrow 0$ spectral line. The simulated maps assumed two subsamples of positions within the clouds and two components. The two components were component 0, with constant physical conditions within each subsample, and component 1, with constant physical conditions within each subsample, except for spatially varying dust and gas temperatures. The two subsamples were defined by the component-1 dust temperature, T_{d1}: those positions with $T_{d1} < 20$ K represent one subsample and the positions with $T_{d1} \geq 20$ K represent the other subsample. The point of the current paper was to apply the models used in Paper I to the simulated maps to see how well those models recover the input values of the physical parameters.

Given that the simulated maps are based on the two-component, two-subsample models, fitting such models to the simulated data in the noise-free case *might* be expected to recover the inputs perfectly. However, even in the noise-free case some input parameters could *not* be recovered. The component-0 and component-1 densities, for example, were an order of magnitude or more different from the inputs. The simulated maps with noise show us that we can obtain the dust-gas temperature difference, ΔT, to within 1 or 2 K *regardless of the specific value of* ΔT. The component zero dust temperature is apparently recovered to within a fraction of a Kelvin, but see Paper III for further discussion of this. Recovery of the component-1 dust temperatures and the gas column densities is accurate to within a few percent for 93% of the points. The other 7% of the points have column densities too high or too low by a factor of about 5. This results in overestimate of only 6-7% in the total mass.

The simple two-component models applied to the simulations has shown what biases can exist in the model results:

1. There are noticeable systematic offsets in the derived component-1 dust temperatures and in the derived column densities from their inputs. These offsets come from forcing a single model curve to fit through the two different subsamples.

2. About 7% of the column densities are wrong by factors of 5, as is the case for the two-subsample, two-component models. Inspite of these systematic errors, the simple two-component models overestimate the total mass of the clouds by only 3 to 6%.

3. Despite the varying the scale factors, the inferred component-1 densities are *all* systematically too low by an order of magnitude or more from the input density.

Keeping these shortcomings in mind gives us reasonable estimates of the parameter value ranges for all the two-component models as applied to the real observations. These ranges are listed in Table 2. The range for the component-1 density is the kind of range roughly expected for LTE emission of the ^{13}CO J = 1 $\rightarrow$ 0 line. The range for the component-1 column density per velocity interval is given, as stated earlier, by the large-scale cloud properties at the low end and by the necessity of optically thin ^{13}CO J = 1 $\rightarrow$ 0 emission at the high end. For component 0, the lower limit is nearly that of the master search grid. (Note that the $c_0 \frac{\mathrm{N_{c0}(^{13}CO)}}{\Delta \mathrm{v_c}}$ product lower limit is indeed *equal* to that of the master search grid, but the $\frac{\mathrm{N_{c0}(^{13}CO)}}{\Delta \mathrm{v_c}}$ *itself* is still slightly larger than that.)

Fitting the one-component models to the simulated data shows that these models can provide reasonable estimates of the column density per velocity interval and volume density (i.e., within factors of 2 or 3) provided that these models are applied to the two different subsamples (i.e. with $\mathrm{T_d}$ below and above 20 K). The estimates of ΔT, however, can be wrong by about 20 K. The one-component models result in mass estimates that are too low by about 40-50%; the continuum-derived mass estimates being worse on average than the ^{13}CO-derived mass estimates due to the higher temperature sensitivity of the continuum observations.

These simulations have provided important insights into the reliability of the model results. Yet other questions need to be addressed:

- What is the effect of the background subtractions used?

- How will dust associated with HI affect the results?

- Does changing the spectral emissivity index β appreciably affect the results?

- Are there alternative kinds of models that would also explain the data?
- How representative are the results of the clouds as a whole, given that the modeled cloud positions only represent 26% of the area of the Orion clouds ?

Paper III examines these questions and discusses the scientific implications of the results.

This work was supported by CONACyT grants #211290-5-0008PE and #202-PY.44676 to W. F. W. at *INAOE.* I am very grateful to W. T. Reach for his comments and support. I owe a great debt of thanks to Y. Fukui and T. Nagahama of Nagoya University for supplying us with the ^{13}CO data that made this work possible. The author is grateful to R. Maddalena and T. Dame, who supplied the map of the peak ^{12}CO J $= 1 \rightarrow 0$ line strengths and provided important calibration information. I thank D. H. Hughes, W. T. Reach, Y. Fukui, M. Greenberg, T. A. .D. Paglione, G. MacLeod, E. Vazquez Semadeni, and others for stimulating and useful discussions.

REFERENCES

COBE Diffuse Infrared Background Experiment (*DIRBE*) Explanatory Supplement 1998, version 2.3, ed. M. G. Hauser, T. Kelsall, D. Leisawitz, and J. Weiland, *COBE* Ref. Pub. 98-A (Greenbelt, MD: NASA/GSFC), available in electronic form from the NSSDC.

Nagahama, T., Mizuno, A., Ogawa, H., and Fukui, Y. 1998, AJ, 116, 336

Wall, W. F. 2006, astro-ph (Paper I)

Wall, W. F. 2006a, astro-ph (Paper III)

This preprint was prepared with the AAS LaTeX macros v5.0.

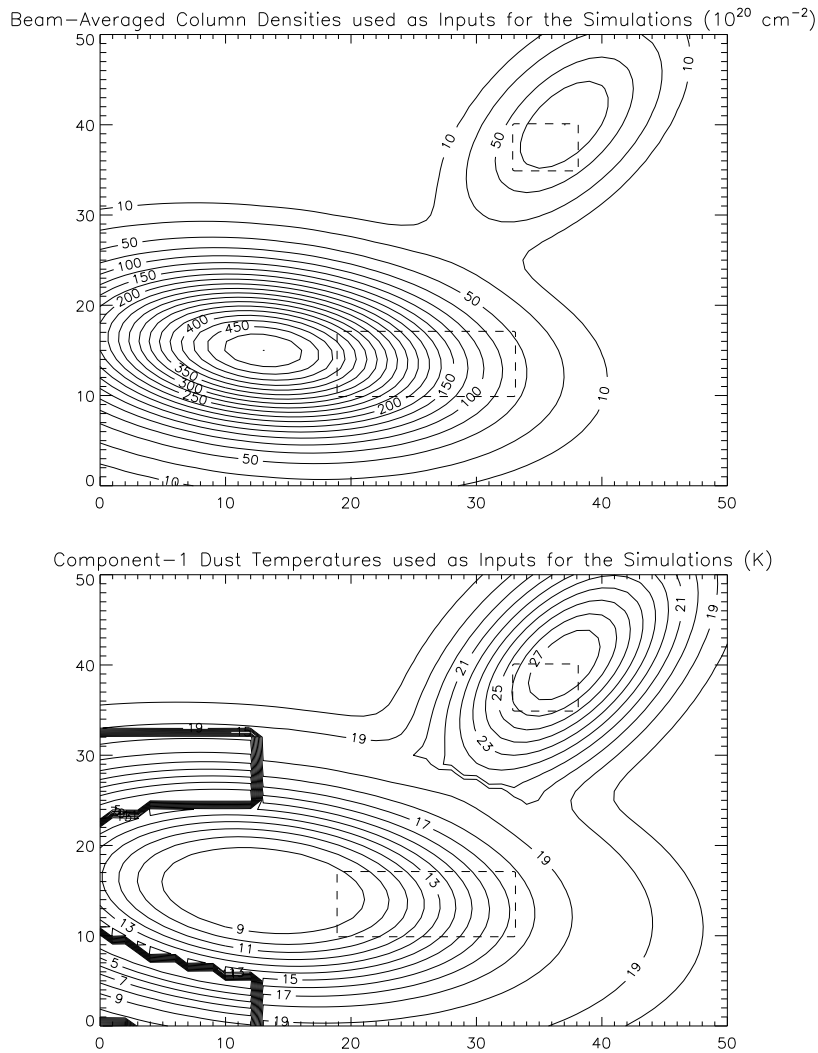

Fig. 1.— The above panels contain contour maps of the inputs for the simulations. The upper panel is the map of beam-averaged column densities in units of 10^{20} *H nuclei* $\cdot$ cm^{-2}. The lower panel is the map of component-1 dust temperatures in Kelvins. Notice that while the column density map consists of two peaks, the temperature has one peak, which coincides with the column density peak in the upper right, and one depression, which coincides with the column density peak in the lower left. The temperature map also has extra low values (between 3 and 12 K) within the boundary of the closely spaced contours that appear on the left side of the map at the bottom and near the middle of the left side. The dashed rectangles illustrate the positions of the patches that have the low noise values in the I(^{13}CO) map.

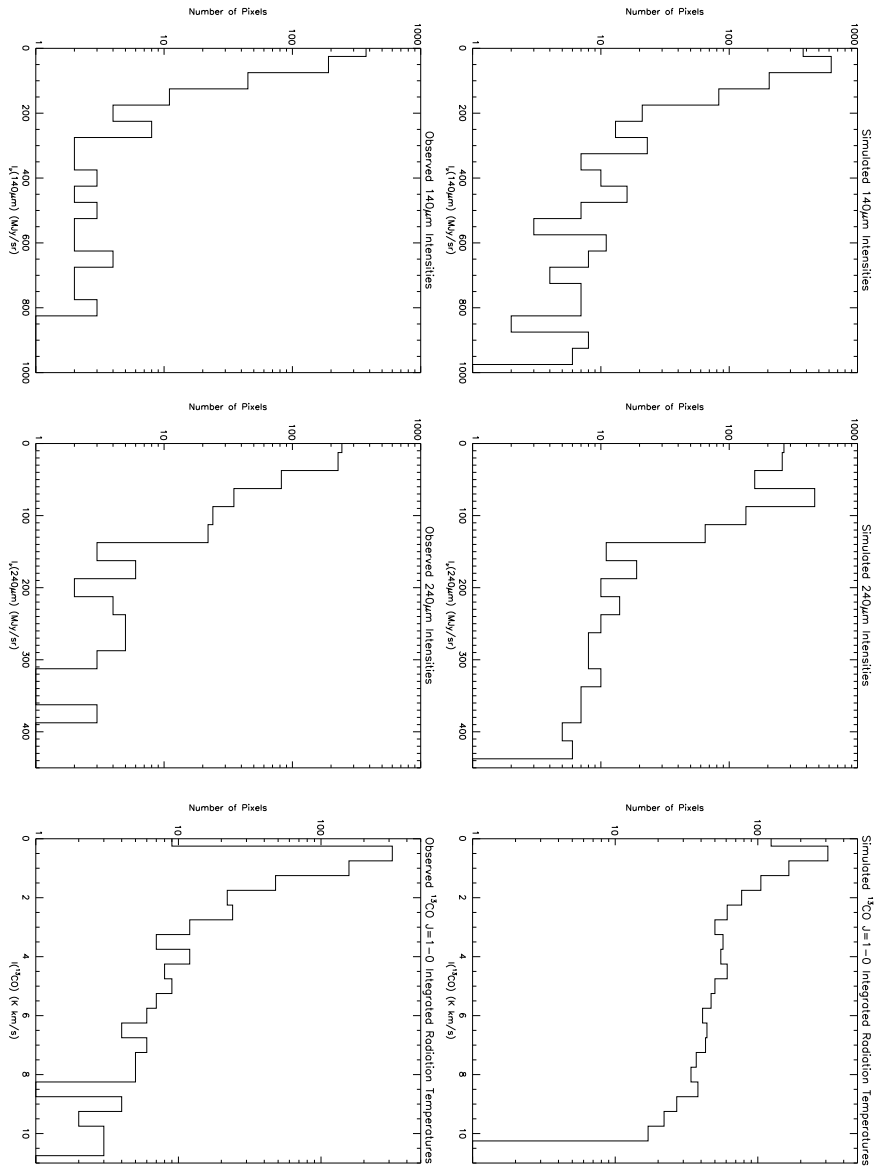

Fig. 2.— Histograms of the simulated and observed intensities for the 140 μm and 240 μm continuum and the ^{13}CO J = 1 $\rightarrow$ 0 line are shown. The upper panels have the histograms of the simulated data and the lower panels have the histograms of the observed data. In all of the panels, only those pixels with intensities above the 5-σ level in $I_\nu(140\,\mu\mathrm{m})$, $I_\nu(240\,\mu\mathrm{m})$, I(^{13}CO) *simultaneously* are represented in the histograms. This corresponds to a total of 1465 pixels in the simulated maps and 674 pixels in the observed maps.

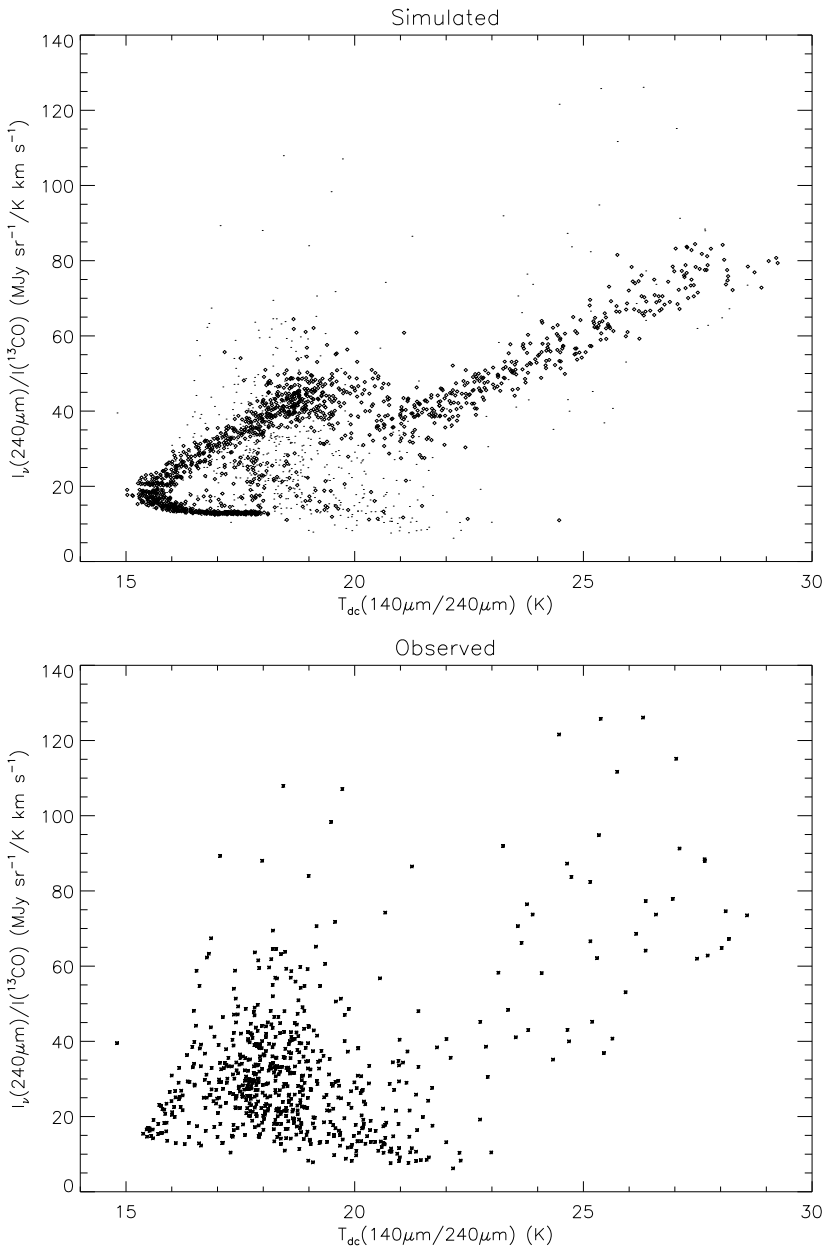

Fig. 3.— Plots of r_{240} versus the 140 μm/240 μm color temperature are shown for the simulations and for the observations. The upper panel is the plot for the simulated data and the lower panel is for the observed data. The error bars are omitted for clarity. The panels only include those pixels with intensities above the 5-σ level in $I_\nu(140\,\mu m)$, $I_\nu(240\,\mu m)$, $I(^{13}CO)$ *simultaneously*.

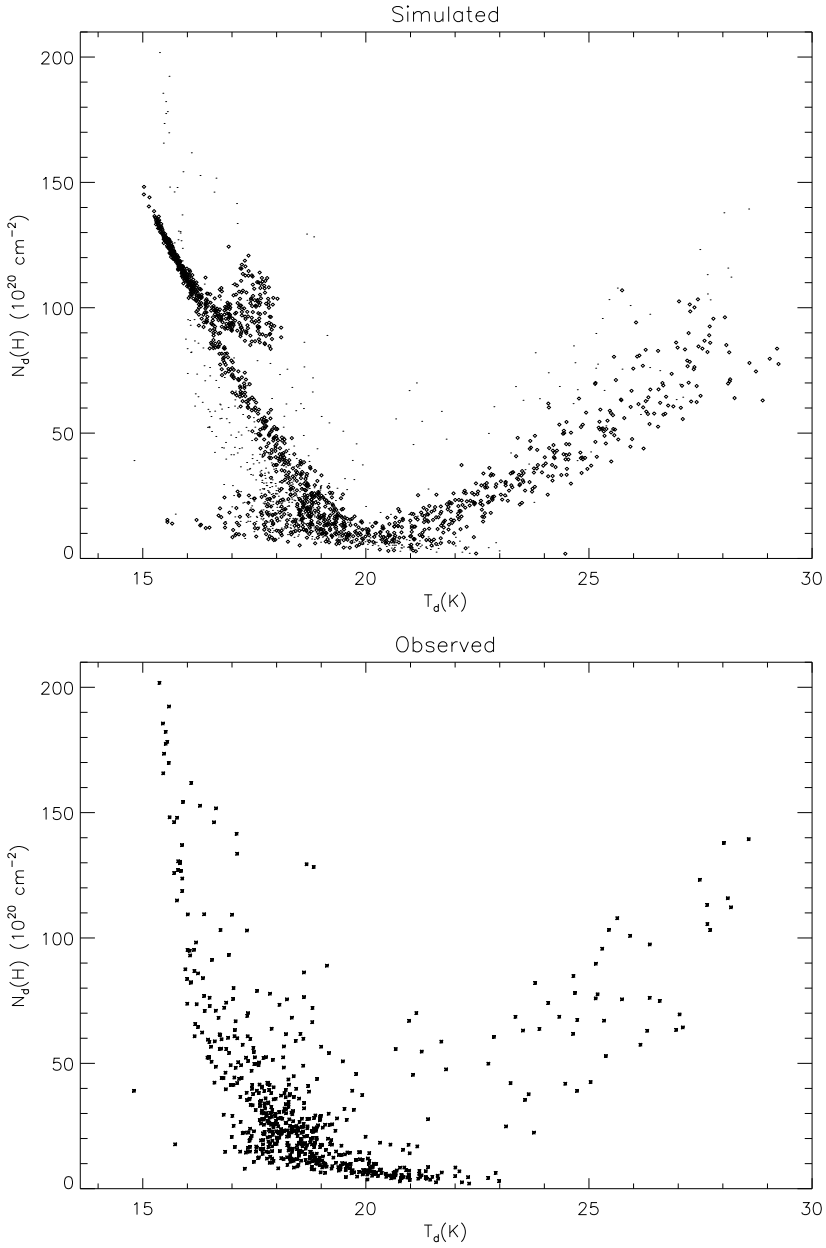

Fig. 4.— Plots of continuum-derived gas column densities, $N_d(H)$, for the one-component case versus the dust temperature are given for the simulations and for the observations. The column densities are in units of 10^{20} *H nuclei* $\cdot$ cm^{-2}. The upper panel is the plot for the simulated data and the lower panel is for the observed data. The panels include omit the error bars for clarity. The panels only include those pixels with intensities above the 5-σ level in $I_\nu(140\,\mu m)$, $I_\nu(240\,\mu m)$, $I(^{13}CO)$ *simultaneously*.

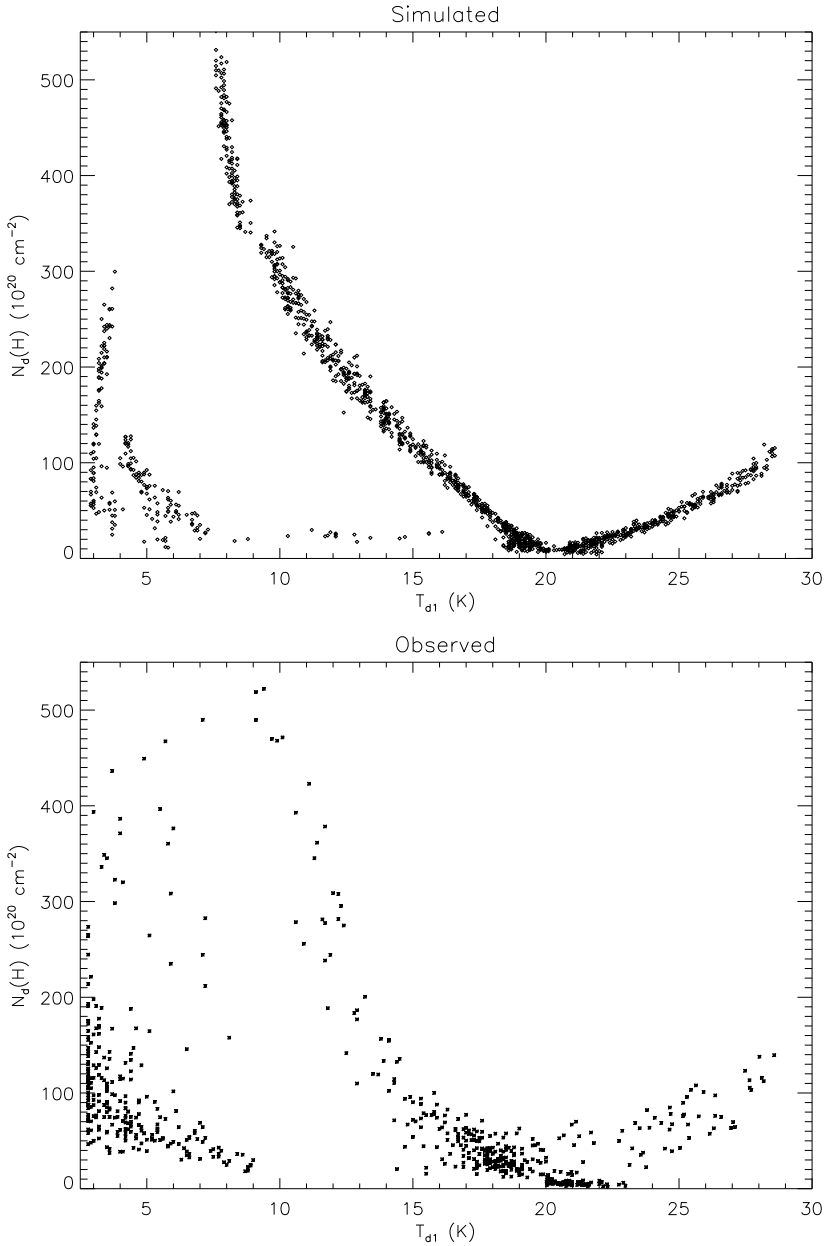

Fig. 5.— Plots of continuum-derived gas column densities, $N_d(H)$, for the two-component, two-subsample case versus the component-1 dust temperature are shown for the simulations and for the observations. The column densities are in units of 10^{20} *H nuclei*$\cdot$ cm^{-2}. The upper panel is the plot for the simulated data and the lower panel is for the observed data. The panels omit the error bars for clarity. The panels only include those pixels with intensities above the 5-σ level in $I_\nu(140\,\mu m)$, $I_\nu(240\,\mu m)$, $I(^{13}CO)$ *simultaneously*.

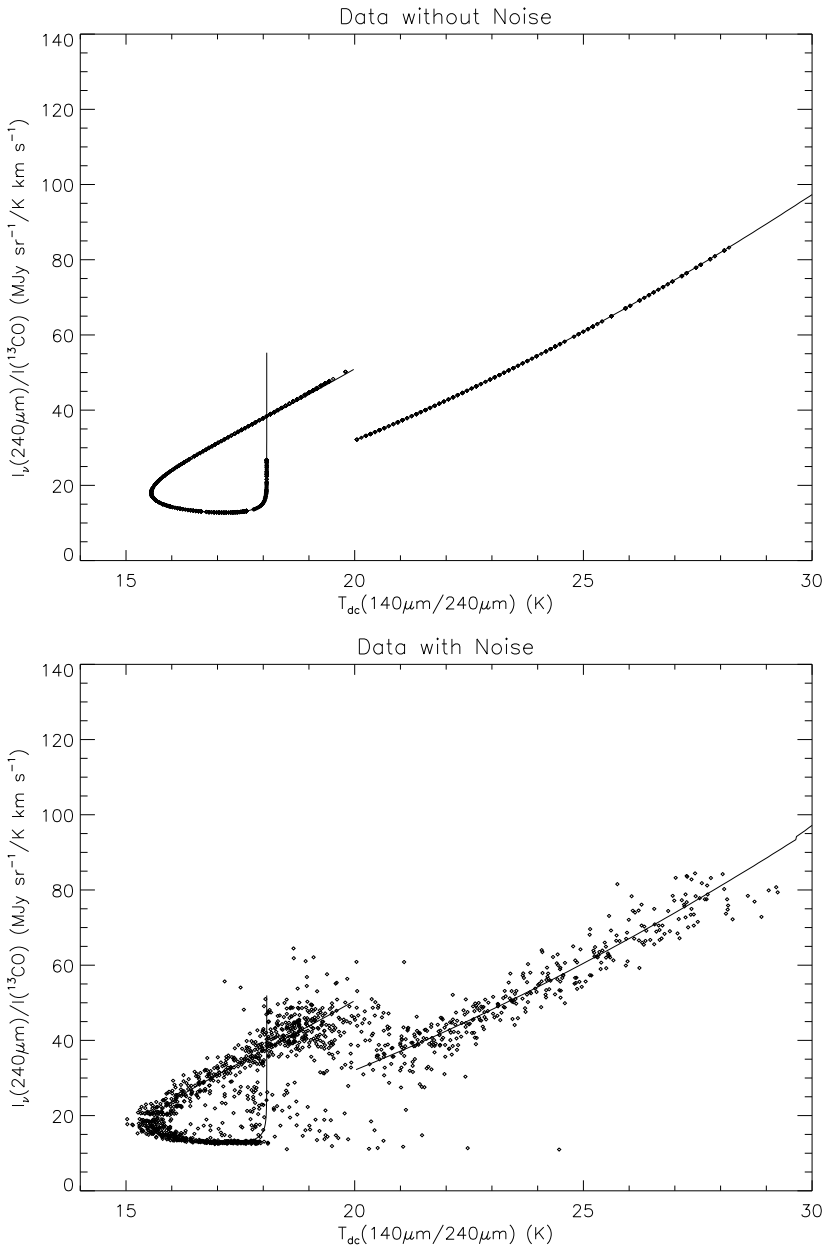

Fig. 6.— Plots of r_{240} versus the $140\,\mu$m/$240\,\mu$m color temperature are shown for the simulations with*out* noise (upper panel) and with noise (lower panel) along with the best-fit model curves for the two-component, two-subsample models. The parameter values used to generate these curves are listed in Table 1. The panels only include those pixels with intensities above the 5-σ level in $I_\nu(140\,\mu m)$, $I_\nu(240\,\mu m)$, $I(^{13}CO)$ *simultaneously*.

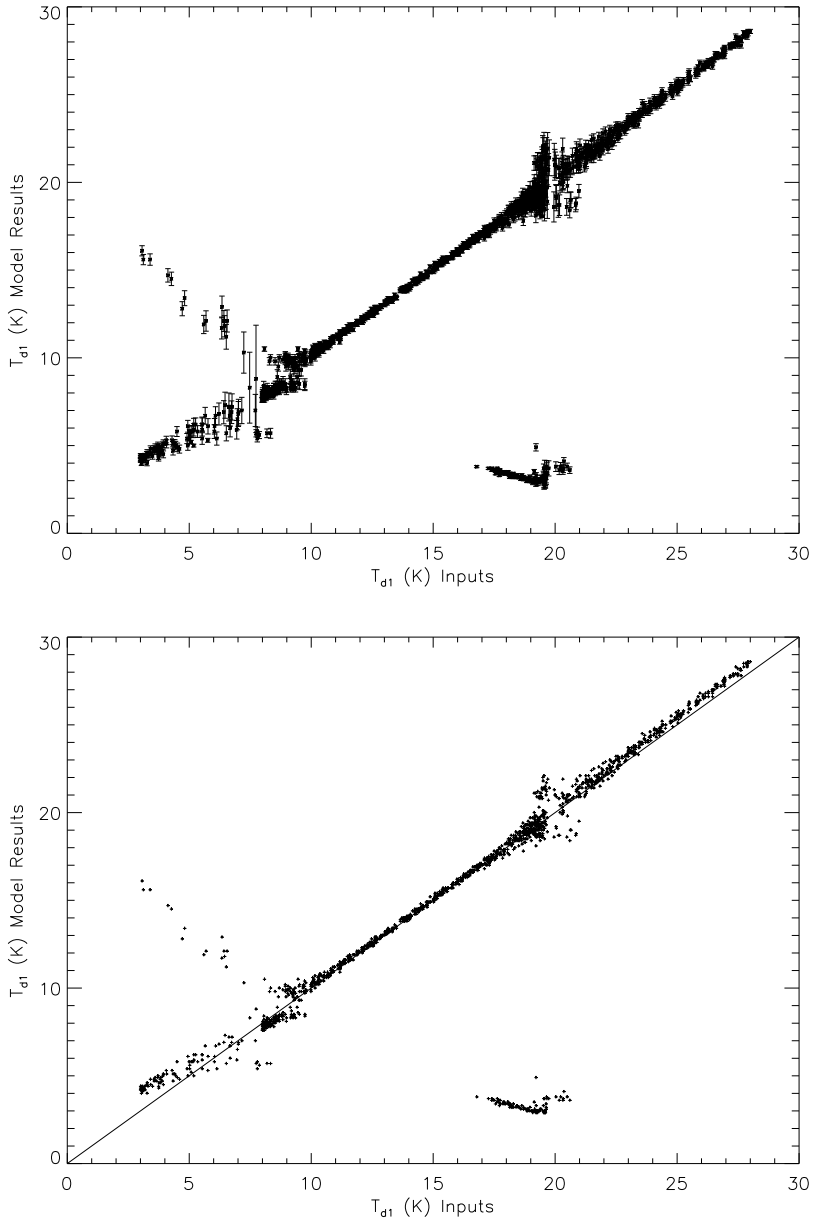

Fig. 7.— The component-1 dust temperature as derived from fitting a two-component, two-subsample model is plotted against the component-1 dust temperature input values for the simulated data. The upper panel includes the error bars in the model results, while the lower panel omits these error bars. The lower panel also includes a solid straight line that represents $T_{d1}(\mathrm{model}) = T_{d1}(\mathrm{input})$ for comparison with the plotted points. The plots only include those pixels with the intensities above the 5-σ level in $I_\nu(140\,\mu\mathrm{m})$, $I_\nu(240\,\mu\mathrm{m})$, $I(^{13}\mathrm{CO})$ *simultaneously*.

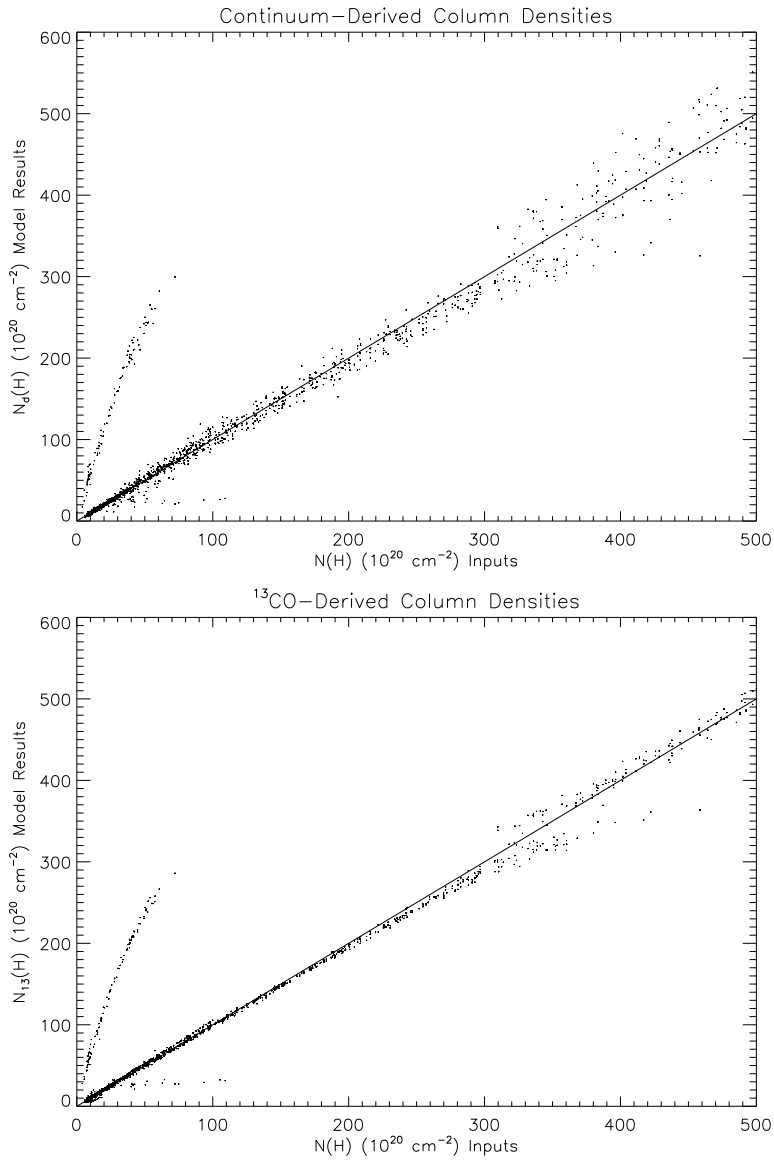

Fig. 8.— Plots of the model gas column densities, $N_d(H)$ and $N_{13}(H)$, for the two-component, two-subsample case versus the input column density values are shown for the simulations. All column densities are in units of 10^{20} *H nuclei* $\cdot$ cm^{-2}. The upper panel is the plot for the continuum-derived column densities, $N_d(H)$, and the lower panel is for the ^{13}CO-derived column densities, $N_{13}(H)$. The panels omit the error bars for clarity. The right panels also include a solid line representing the hypothetical case of agreement between the inputs and the model results (i.e. slope=1 and y-intercept=0). The panels only include those pixels with intensities above the 5-σ level in $I_\nu(140\,\mu m)$, $I_\nu(240\,\mu m)$, $I(^{13}CO)$ *simultaneously*.

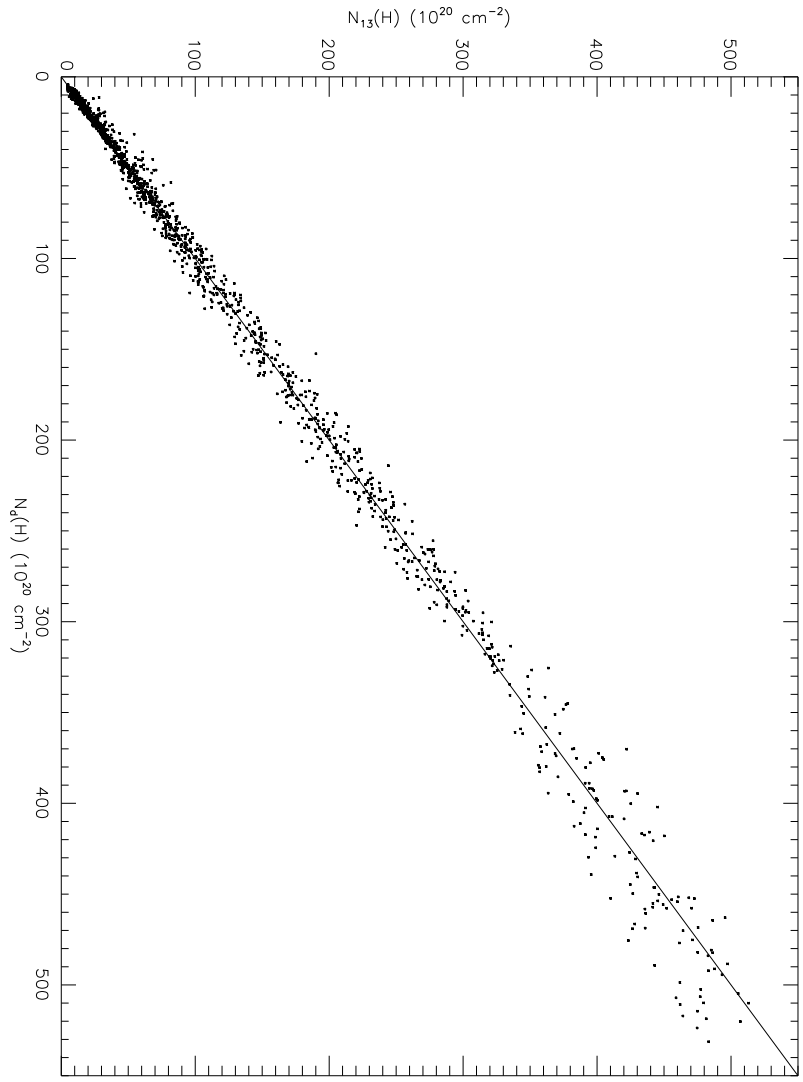

Fig. 9.— Plot of the continuum-derived gas column densities, $N_d(H)$, versus the ^{13}CO-derived gas column densities, $N_{13}(H)$, is shown for the simulations, where the column densities were derived using the parameters from the best-fit two-component, two-subsample models. All column densities are in units of 10^{20} *H nuclei* $\cdot$ cm^{-2}. The plot includes a solid straight line that represents $N_{13}(H) = N_d(H)$ for comparison with the plotted points. The plots only include those pixels with the intensities above the 5-σ level in $I_\nu(140\,\mu m)$, $I_\nu(240\,\mu m)$, $I(^{13}CO)$ *simultaneously*. The error bars are omitted for clarity.

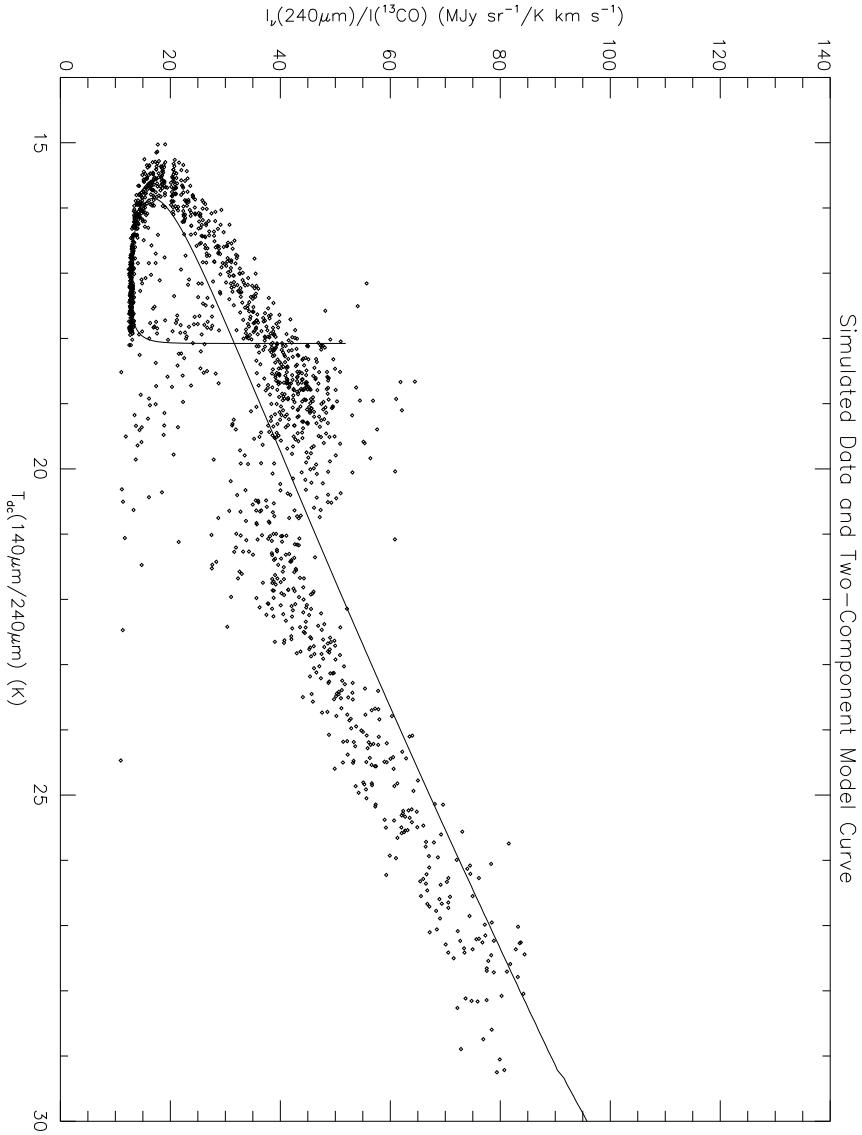

Fig. 10.— Plot of r_{240} versus the $140\,\mu$m/$240\,\mu$m color temperature is shown for the simulations along with the best-fit model curves for the two-component models. The plots only include those pixels with the intensities above the 5-σ level in $I_\nu(140\,\mu\mathrm{m})$, $I_\nu(240\,\mu\mathrm{m})$, $I(^{13}\mathrm{CO})$ *simultaneously*. Error bars have been omitted for clarity.

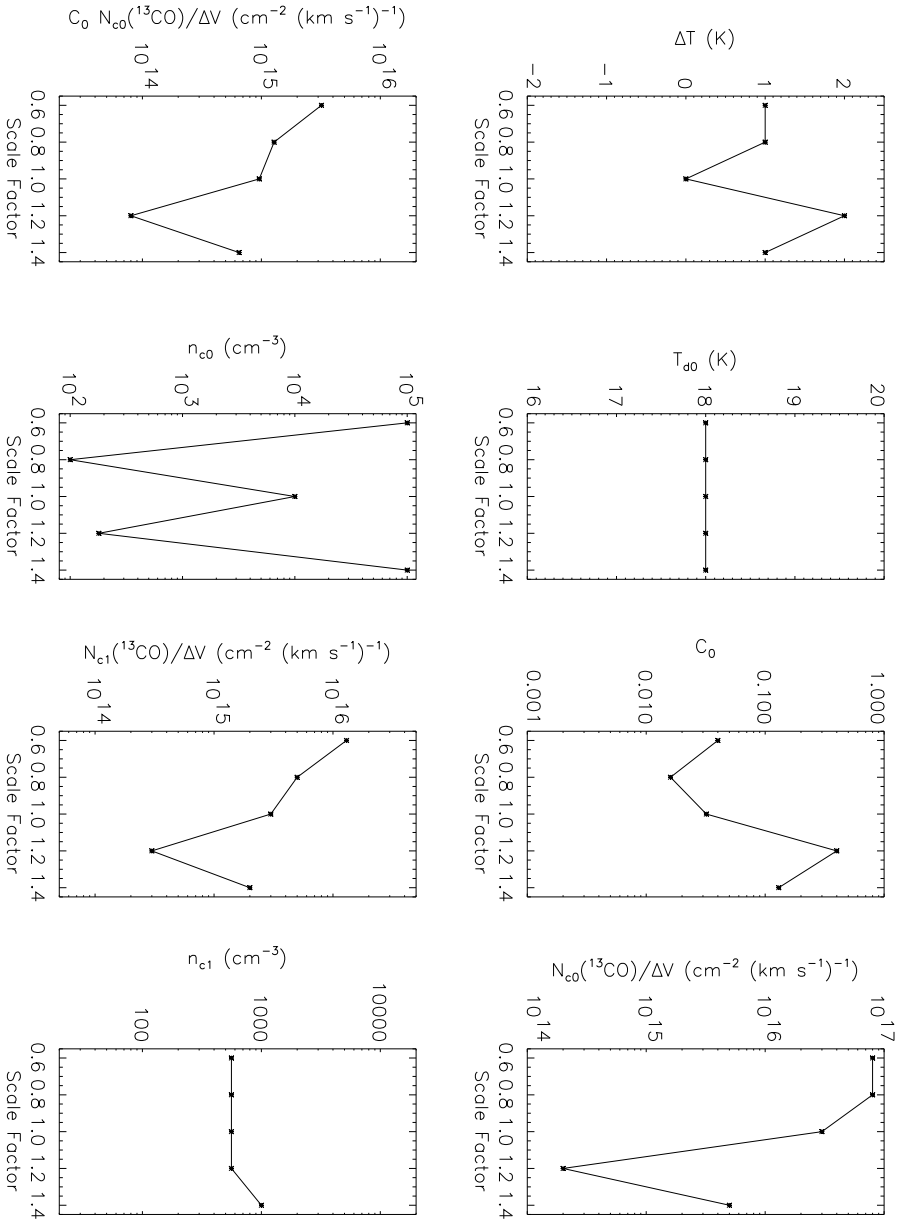

Fig. 11.— The effect of the systematic uncertainties on the resultant parameters from the fits of the two-component, LVG model curves to the simulated data is shown. The effect of these uncertainties was tested by applying the scale factors 0.6, 0.8, 1.0, 1.2, and 1.4 to the model curves and fitting the parameters for each scale factor. Except for the plots for ΔT and T_{d0}, all plots are semi-logarithmic where the vertical axes cover the about the same logarithmic difference in range (about 3 orders of magnitude). This allows easy visual determination of which parameters have the smallest systematic uncertainties.

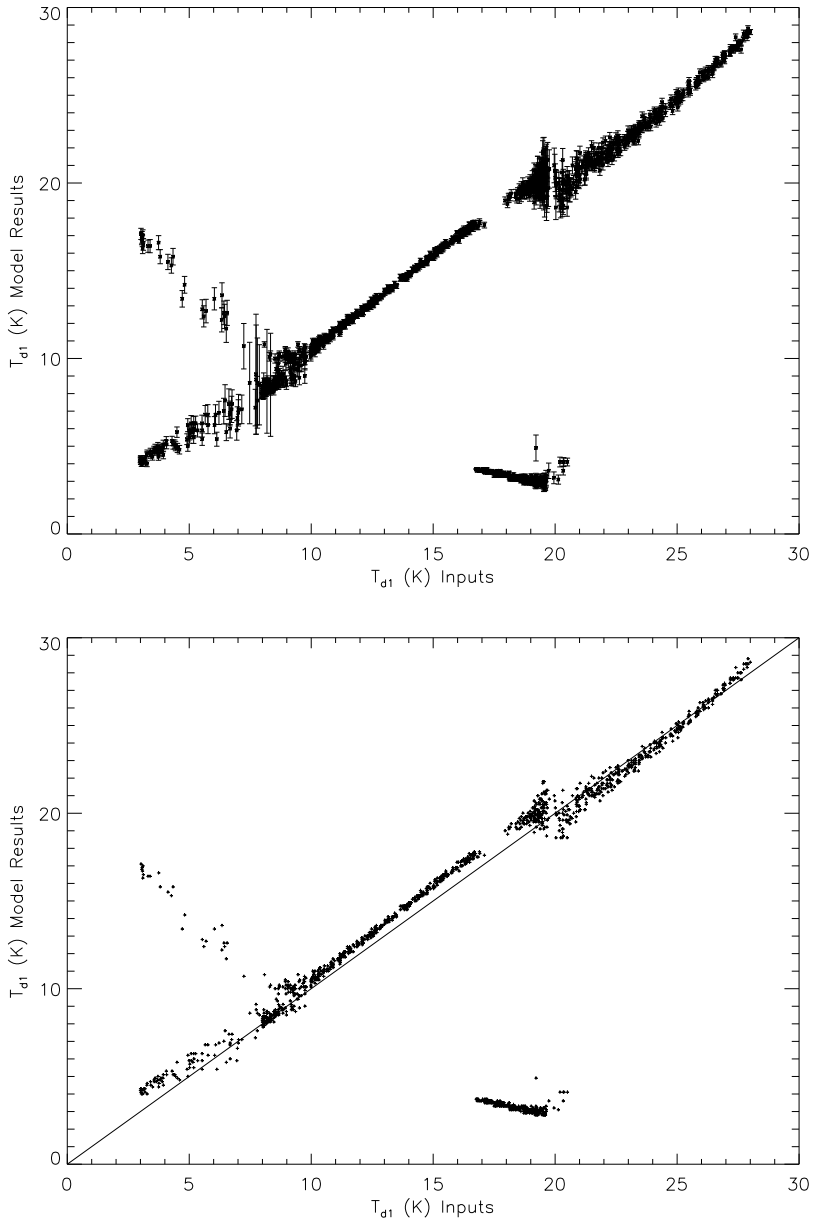

Fig. 12.— The component-1 dust temperature as derived from fitting a two-component model is plotted against the component-1 dust temperature input values for the simulated data. The upper panel includes the error bars in the model results, while the lower panel omits these error bars. The lower panel also includes a solid straight line that represents T_{d1}(model) = T_{d1}(input) for comparison with the plotted points. The plots only include those pixels with the intensities above the 5-σ level in $I_\nu(140\,\mu m)$, $I_\nu(240\,\mu m)$, I(^{13}CO) *simultaneously*.

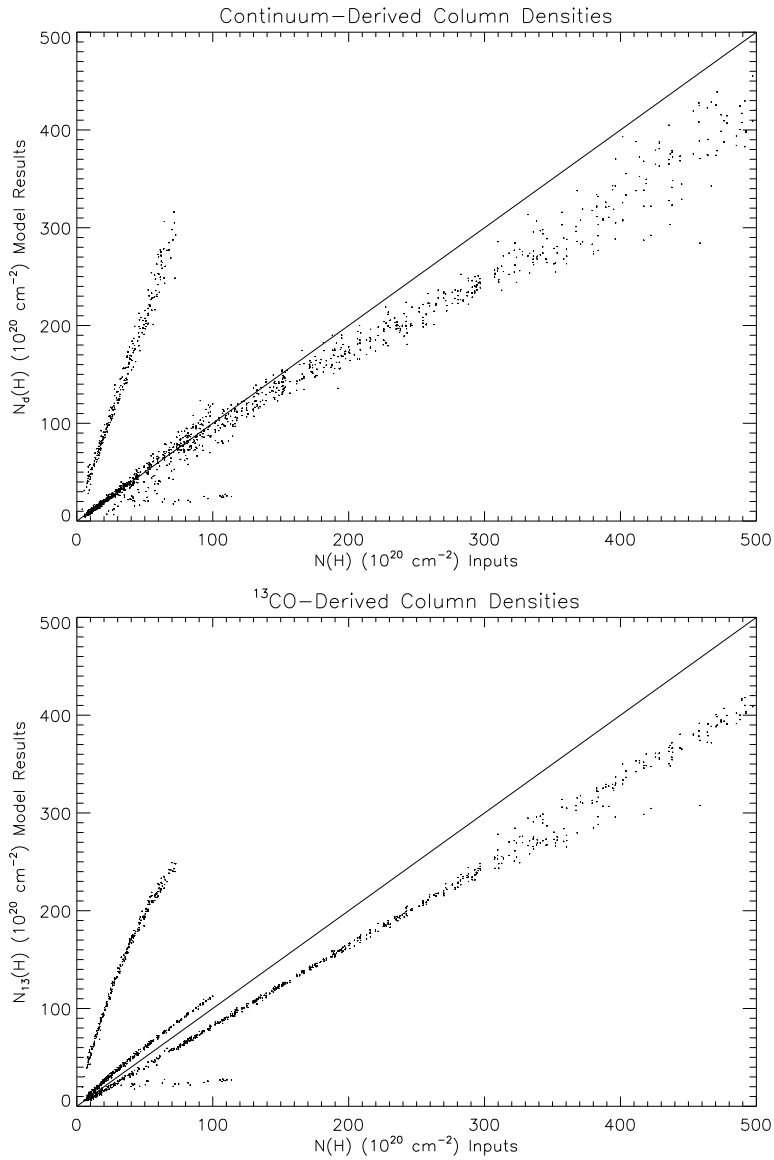

Fig. 13.— Plots of the model gas column densities, $N_d(H)$ and $N_{13}(H)$, for the two-component case versus the input column density values are shown for the simulations. All column densities are in units of 10^{20} *H nuclei* $\cdot$ cm^{-2}. The upper panel is the plot for the continuum-derived column densities, $N_d(H)$, and the lower panel is for the ^{13}CO-derived column densities, $N_{13}(H)$. The panels omit the error bars for clarity. A solid line is included in each panel that represents the hypothetical case of agreement between the inputs and the model results (i.e. slope=1 and y-intercept=0). The panels only include those pixels with intensities above the 5-σ level in $I_\nu(140\,\mu m)$, $I_\nu(240\,\mu m)$, I(^{13}CO) *simultaneously*.

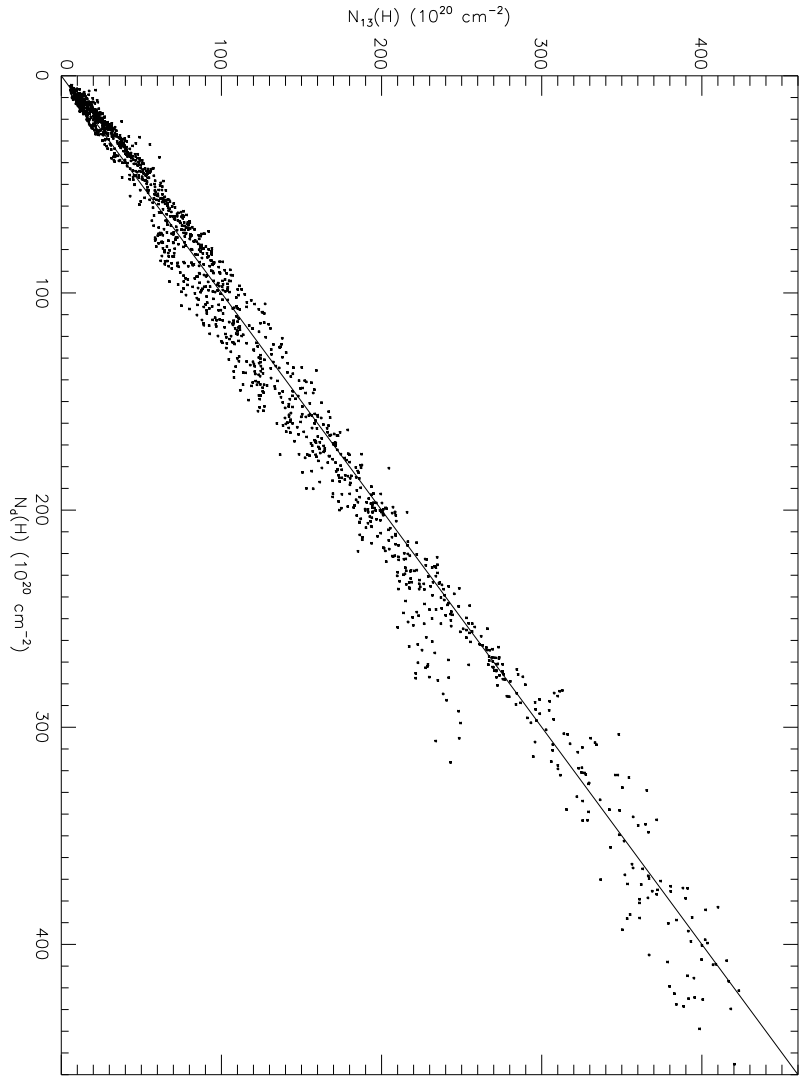

Fig. 14.— Plot of the continuum-derived gas column densities, $N_d(H)$, versus the ^{13}CO-derived gas column densities, $N_{13}(H)$, is shown for the simulations, where the column densities were derived using the parameters from the best-fit two-component models. All column densities are in units of 10^{20} *H nuclei* $\cdot$ cm^{-2}. A solid straight line is included that represents $N_{13}(H) = N_d(H)$ for comparison with the plotted points. The plots only include those pixels with the intensities above the 5-σ level in $I_\nu(140\,\mu m)$, $I_\nu(240\,\mu m)$, $I(^{13}CO)$ *simultaneously*. Error bars are omitted for clarity.

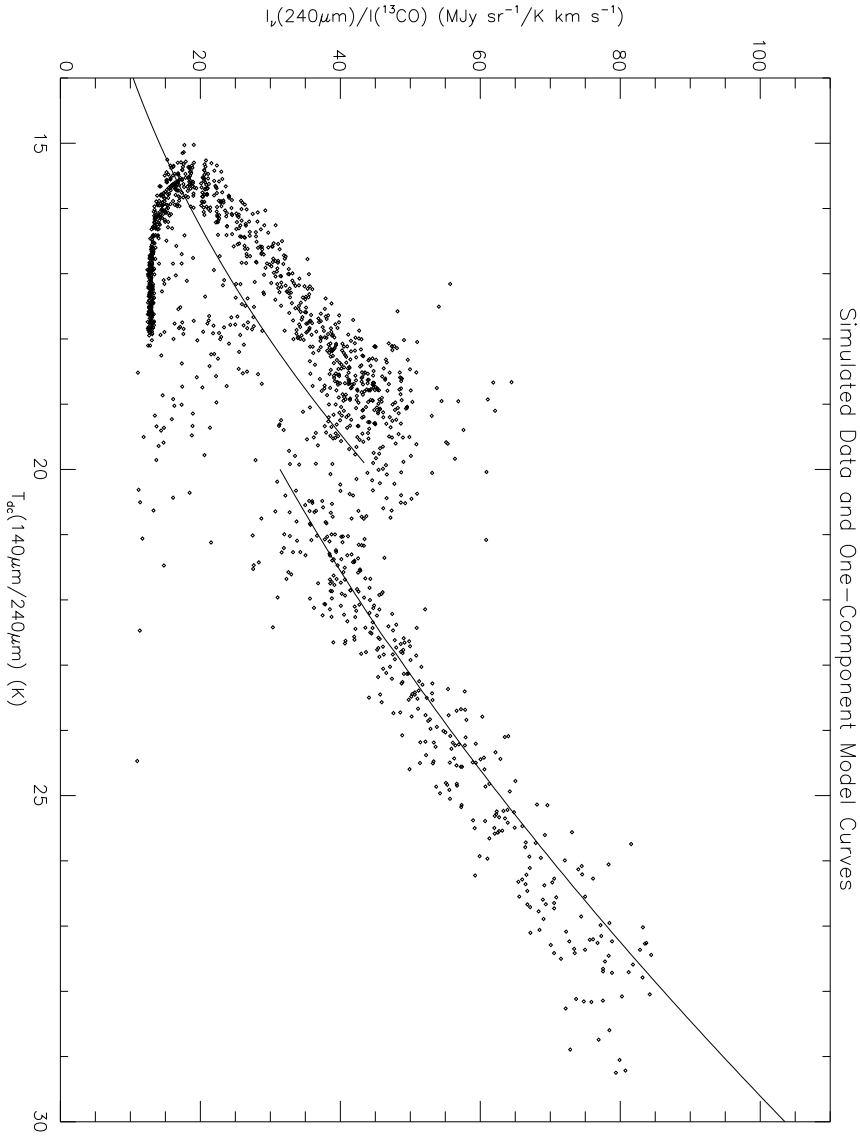

Fig. 15.— Plot of r_{240} versus the dust temperature is shown for the simulations along with the best-fit model curves for the one-component models. These models were applied to the $T_d < 20\,K$ and $T_d \geq 20\,K$ subsamples separately. The plots only include those pixels with the intensities above the 5-σ level in $I_\nu(140\,\mu m)$, $I_\nu(240\,\mu m)$, $I(^{13}CO)$ *simultaneously*. Error bars have been omitted for clarity.

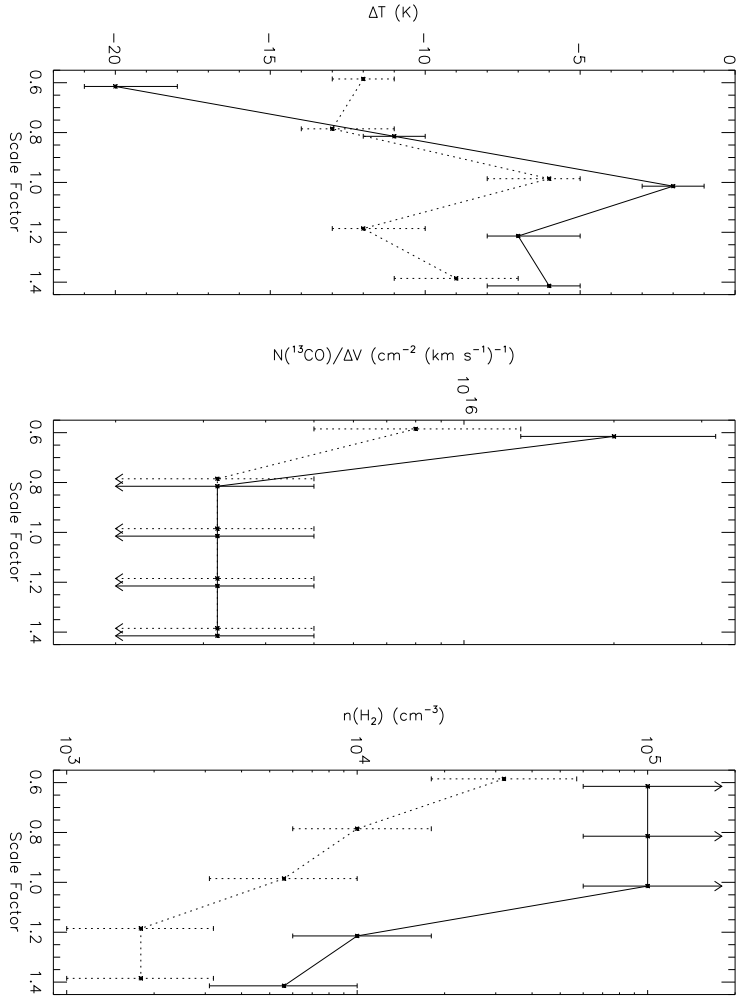

Fig. 16.— The effect of the systematic uncertainties on the resultant parameters from the fits of the LVG model curves to the simulated data is shown. The effect of these uncertainties was tested by applying scale factors to the model curves and fitting the parameters for each scale factor. The left panel shows the resultant ΔT values, the center panel shows the resultant N(^{13}CO)/Δv values, and the right panel shows the n(H_2) values. The solid line in each panel represents the resultant parameter values for the fits to the subsample of points with $T_d < 20\,K$. The dotted line represents the resultant parameter values for the fits to the subsample of data with $T_d \geq 20\,K$. Notice that the plotted points have been slightly displaced horizontally from their true scale factor values for clarity. The error bars represent the formal error bars for each model fit and are the minimum grid spacing, for the grid of LVG models used, necessary to increase χ^2 by a *minimum* of χ^2_ν. These formal errors are therefore very conservative estimates of the true formal errors.

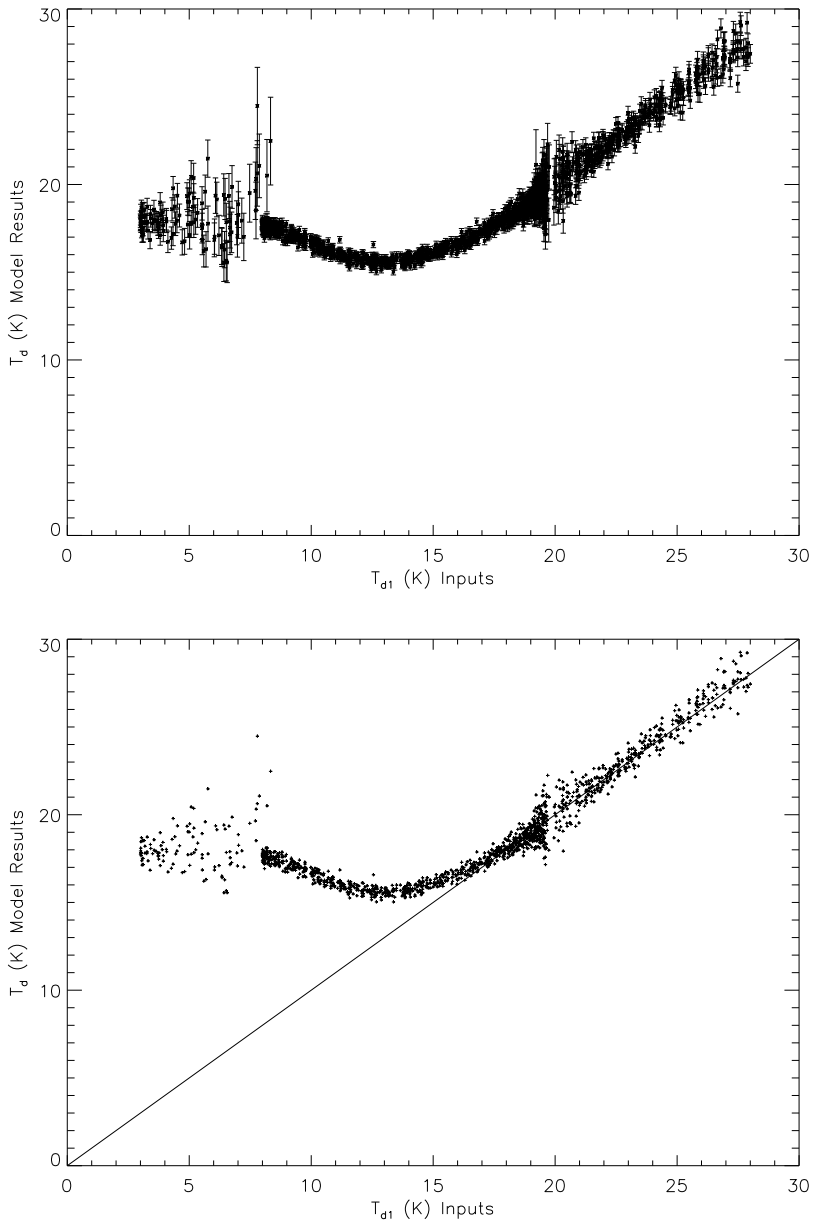

Fig. 17.— The dust temperature as derived from fitting a one-component model is plotted against the component-1 dust temperature input values for the simulated data. The upper panel includes the error bars in the model results, while the lower panel omits these error bars. The lower panel also includes a solid straight line that represents $T_{d1}(\mathrm{model}) = T_{d1}(\mathrm{input})$ for comparison with the plotted points. The plots only include those pixels with the intensities above the 5-σ level in $I_\nu(140\,\mu\mathrm{m})$, $I_\nu(240\,\mu\mathrm{m})$, $I(^{13}\mathrm{CO})$ *simultaneously*.

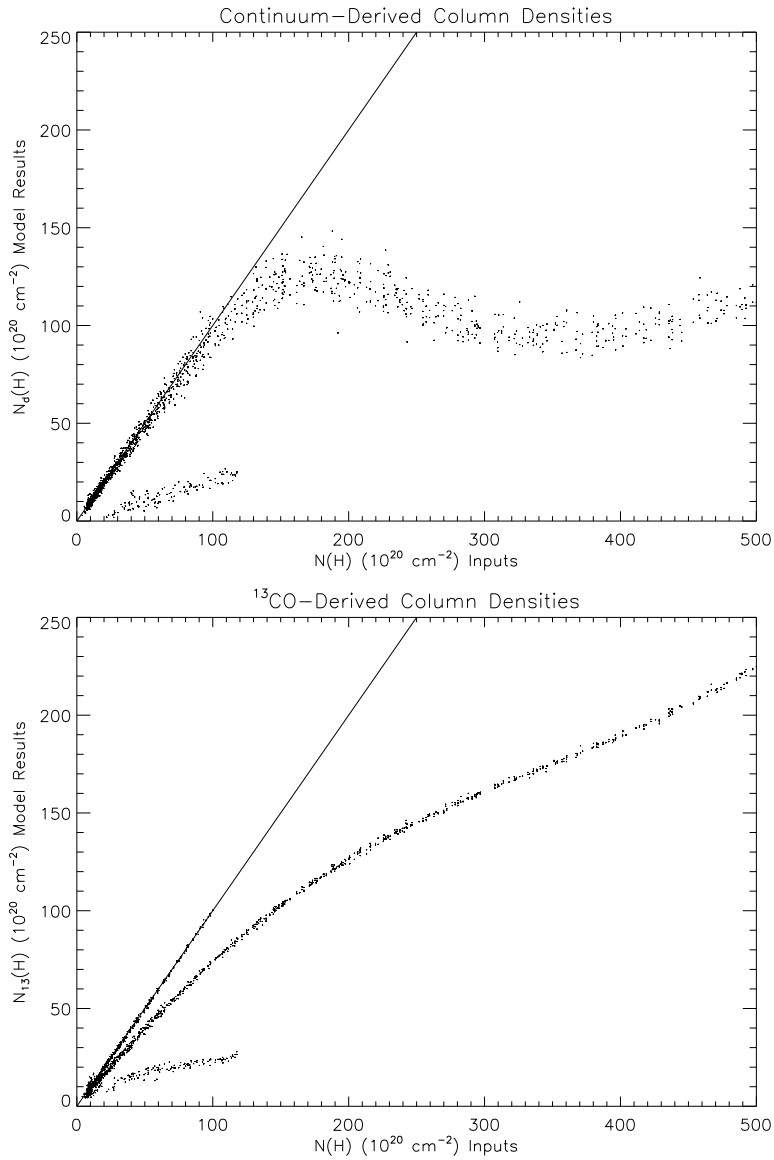

Fig. 18.— Plots of the model gas column densities, $N_d(H)$ and $N_{13}(H)$, for the one-component case versus the input column density values are shown for the simulations. All column densities are in units of 10^{20} *H nuclei* $\cdot$ cm^{-2}. The upper panel is the plot for the continuum-derived column densities, $N_d(H)$, and the lower panel is for the ^{13}CO-derived column densities, $N_{13}(H)$. The panels omit the error bars for clarity. A solid line is included in each that represents the hypothetical case of agreement between the inputs and the model results (i.e. slope=1 and y-intercept=0). The panels only include those pixels with intensities above the 5-σ level in $I_\nu(140\,\mu m)$, $I_\nu(240\,\mu m)$, $I(^{13}CO)$ *simultaneously*.

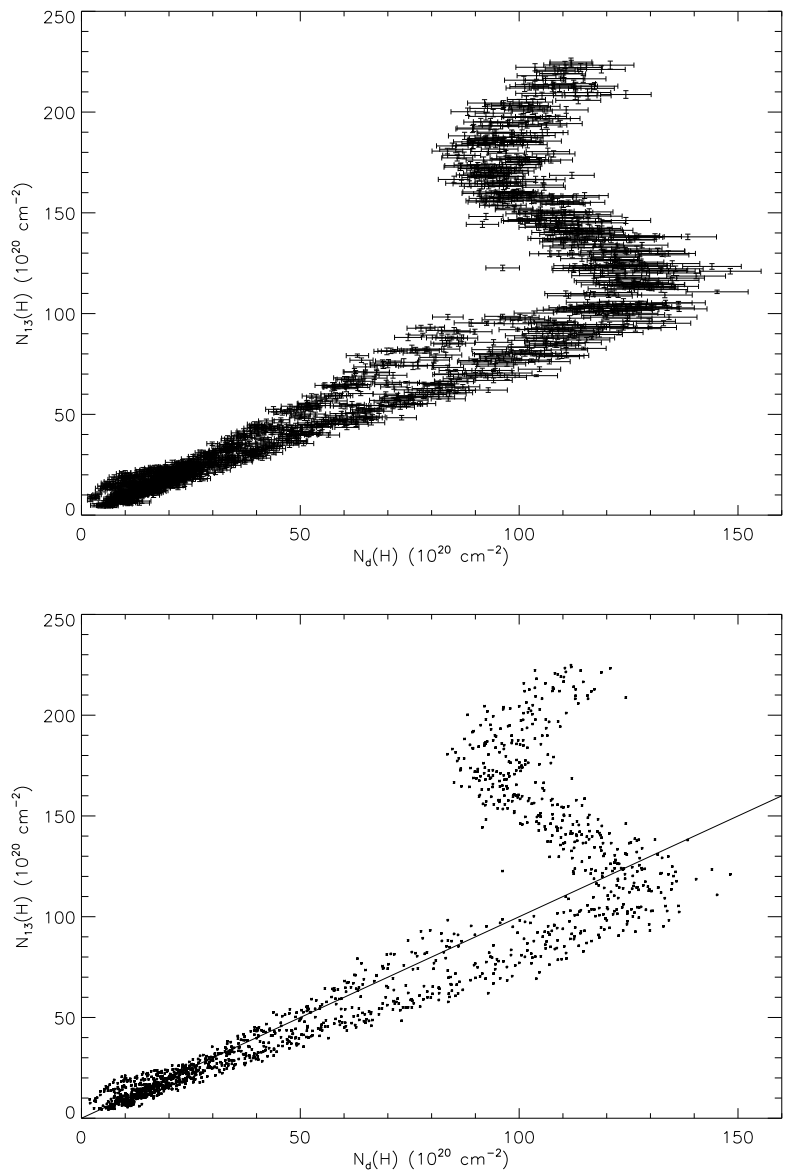

Fig. 19.— Plots of the continuum-derived gas column densities, $N_d(H)$, versus the ^{13}CO-derived gas column densities, $N_{13}(H)$, are shown for the simulations, where the column densities were derived using the parameters from the best-fit one-component models. All column densities are in units of 10^{20} *H nuclei* $\cdot$ cm^{-2}. The upper panel includes the error bars in the model results, while the lower panel omits these error bars. The lower panel also includes a solid straight line that represents $N_{13}(H) = N_d(H)$ for comparison with the plotted points. The plots only include those pixels with the intensities above the 5-σ level in $I_\nu(140\,\mu m)$, $I_\nu(240\,\mu m)$, $I(^{13}CO)$ *simultaneously*.

Table 1. Parameter Values for the Simulations

Parameter	Input Values		Model Results (Noise Free)		Model Results (with Noise)	
	$T_{dc} < 20\,K$	$T_{dc} \geq 20\,K$	$T_{dc} < 20\,K$[a]	$T_{dc} \geq 20\,K$[b]	$T_{dc} < 20\,K$[c]	$T_{dc} \geq 20\,K$[d]
ΔT[e]	0	0	-1	0	-1	2
c_0[f]	1.0	0.4	0.063	0.63	1.6	0.13
T_{d0}[e]	18	18	18	18	18	18
$\frac{N_{c0}(^{13}CO)}{\Delta v_c}$[g]	5.0×10^{15}	5.0×10^{14}	5.0×10^{16}	3.2×10^{14}	2.0×10^{15}	5.0×10^{15}
n_{c0}[h]	3.2×10^{4}	1.0×10^{4}	5.6×10^{1}	1.0×10^{4}	3.2×10^{1}	1.0×10^{4}
$c_0 \frac{N_{c0}(^{13}CO)}{\Delta v_c}$[g]	5.0×10^{15}	2.0×10^{14}	3.2×10^{15}	2.0×10^{14}	3.2×10^{15}	6.5×10^{14}
$\frac{N_{c1}(^{13}CO)}{\Delta v_c}$[g]	2.0×10^{16}	5.0×10^{15}	1.3×10^{16}	5.0×10^{15}	1.3×10^{16}	3.2×10^{15}
n_{c1}[h]	3.2×10^{4}	5.6×10^{3}	5.6×10^{3}	5.6×10^{3}	5.6×10^{3}	1.0×10^{4}
χ^2_ν	—	—	1.59×10^{-2}	6.23×10^{-4}	1.15	1.90
ν	—	—	1129	366	1066	389

[a]Formal relative errors are $\leq 1 \times 10^{-5}$ for all parameters, except ΔT and T_{d0}, which have formal absolute errors of $\leq 1 \times 10^{-5}\,K$.

[b]Formal relative errors are $\leq 1 \times 10^{-1}$ for all parameters, except ΔT and T_{d0}. ΔT has a formal absolute error of $\leq 1 \times 10^{-1}\,K$. T_{d0} was simply adopted to be 18 K.

[c]Formal relative errors are $\leq 3 \times 10^{-5}$ for all parameters, except ΔT and T_{d0}, which have formal absolute errors of $\leq 3 \times 10^{-5}\,K$.

[d]Formal relative errors are $\leq 2 \times 10^{-2}$ for all parameters, except ΔT and T_{d0}. ΔT has a formal absolute error of $\leq 2 \times 10^{-2}\,K$. T_{d0} was simply adopted to be 18 K.

[e]In units of Kelvins.

[f]Dimensionless.

[g]In units of ^{13}CO molecules $\cdot\, cm^{-2} \cdot (km \cdot s^{-1})^{-1}$.

[h]In units of H_2 molecules $\cdot\, cm^{-3}$.

Table 2. Best Estimates of Parameter Value Ranges[a]

Parameter	Range of Values
ΔT^{b}	-1 to $+2\,K$
T_{d0}	$18\,K^{c}$
$c_0 \frac{N_{c0}(^{13}CO)}{\Delta v_c}$	2.0×10^{14} to 5.0×10^{15} ^{13}CO $cm^{-2} \cdot (km \cdot s^{-1})^{-1}$
n_{c0}	$\gtrsim 20$ H_2 cm^{-3}
$\frac{N_{c1}(^{13}CO)}{\Delta v_c}$[d]	3×10^{15} to 2×10^{16} ^{13}CO $cm^{-2} \cdot (km \cdot s^{-1})^{-1}$
n_{c1}	$\gtrsim few \times 10^{3}$ H_2 cm^{-3}

[a]See Subsection 2.2 for details.

[b]Assuming two-component models applied to *both* subsamples.

[c]The uncertainty of this will be dealt with in Paper III.

[d]For the two-component models applied to the two subsamples, the $\frac{N_{c1}(^{13}CO)}{\Delta v_c}$ value would be at the higher end of this range for the $T_{dc} < 20\,K$ subsample and at the lower end for the $T_{dc} \geq 20\,K$ subsample.